Pre-eruptive conditions at satellite vent eruptions at Teide-Pico Viejo complex (Tenerife, Canary Islands)

Olaya Dorado, Joan Andújar, Joan Martí, Adelina Geyer

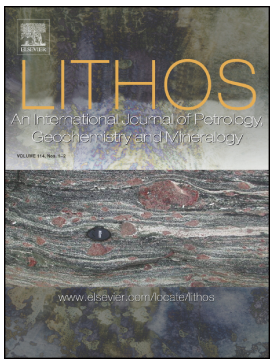

Pre-eruptive conditions at satellite vent eruptions at Teide-Pico Viejo complex (Tenerife, Canary Islands)

Olaya Dorado, Joan Andújar, Joan Martí, Adelina Geyer

PII: S0024-4937(21)00229-2

DOI: https://doi.org/10.1016/j.lithos.2021.106193

Reference: LITHOS 106193

To appear in: *LITHOS*

Received date: 20 November 2020

Revised date: 19 April 2021

Accepted date: 24 April 2021

Please cite this article as: O. Dorado, J. Andújar, J. Martí, et al., Pre-eruptive conditions at satellite vent eruptions at Teide-Pico Viejo complex (Tenerife, Canary Islands), *LITHOS* (2021), https://doi.org/10.1016/j.lithos.2021.106193

Pre-eruptive conditions at satellite vent eruptions at Teide-Pico Viejo complex (Tenerife, Canary Islands)

Olaya Dorado[1,2], Joan Andújar[3], Joan Martí[1], Adelina Geyer[1]

[1]Geosciences Barcelona (GEO3BCN-CSIC) C/Lluís Solé i Sabarís s/n, 08028, Barcelona, Spain.

[2]Departament de Mineralogia, Petrología i Geologia Aplicada, Facultat de Ciències de la Terra, Universitat de Barcelona, c/Martí Franquès s/n, 08028 Barcelona, Spain.

[3]Institut des Sciences de la Terre d'Orléans (ISTO) UMR 7327, Université d'Orléans-CNRS-BRGM, Campus Géosciences, 1A rue de la Férollerie, 45071 Orleans, Cedex 2, France.

Email addresses:

Olaya Dorado: odorado@geo3bcn.csic.es

Joan Andújar: juan.andujar@cnrs-orleans.fr

Joan Martí: jmarti@geo3bcn.csic.es

Adelina Geyer: ageyer@geo3bcn.csic.es

Corresponding Author:

Olaya Dorado García, Graduate Researcher.

Geosciences Barcelona (GEO3BCN-CSIC).

C/Lluís Solé i Sabarís s/n, 08028, Barcelona, Spain.

Tel. +34 93 409 5410 ext. 257

Email: odorado@geo3bcn.csic.es

Abstract

The Teide-Pico Viejo (T-PV) stratovolcanoes constitute one of the most potentially active volcanic complexes in Europe. T-PV was traditionally considered as a non-explosive system, but recent studies have pointed out the explosive character of their phonolitic magmas, including plinian and subplinian eruptions and the generation of pyroclastic density currents, as is evidenced in the volcanological record of the last 30 kyr. This explosive activity is mostly associated with satellite dome-like vents, which are characterised by presenting progressive transitions between explosive and effusive activity. In order to

improve our understanding of these types of eruptions and their controlling mechanisms, we conducted a petrological and mineral characterisation of the products from the different eruptive phases of Pico Cabras dome. This permitted us to constrain the pre-eruptive conditions of the magma and to infer the potential factors that control the changes in the volcanic activity of dome-forming eruptions at T-PV and, in particular, the transition between explosive and effusive phases.

Feldspar (anorthoclase and sanidine), clinopyroxene (diopside and augite), biotite, amphibole (kaersutite), magnetite, ilmenite, sodalite, and glass samples were analysed using EPMA and Micro-XRF. Our results suggest the presence of a compositionally, thermally, and volatile stratified magma chamber at 100 ± 50 MPa prior to the Pico Cabras eruption (between 9210 and 5911 years BP), which was characterised by a progressive change in the style of activity, from an efficiently fragmented magma dispersed by a sustained plume, to a poorly-fragmented, low-height, non-convective fountain (forming the fountain-fed lava dome) to a glass-bearing lava flow activity. The transition in the eruptive style was controlled by changes in temperature and amount of volatiles dissolved in the phonolitic melt (i.e., differences in magma rheology). The initial explosive phase was related to the emission of highly evolved phonolitic magma ponding at 725-800 ºC while containing 3.5-5 wt.% H_2O and located in the upper part of the magma reservoir. The magma that fed the phonolitic lava flow formed the main body of the reservoir and was stored below the preceding melt at 880 ± 30 ºC and with 2.5-3 wt.% H_2O dissolved. Feldspar zonation suggests that the eruption was triggered by the intrusion of hotter mafic magma at the base of the phonolitic chamber, which induced the overturn of the interior of the reservoir. However, the interaction between the internal magmas was short enough to prevent the hybridization phenomena among them. The compositions of some feldspars from the most explosive phase are equivalent to those found in the El Abrigo eruption, the last caldera-forming episode (ca. 190 ka), demonstrating that T-

PV volcanic system can already produce evolved and highly explosive magmas, a factor that should be considered in future hazard assessment for Tenerife.

Keywords: Teide-Pico Viejo, Tenerife, dome, phonolite, explosive-effusive

1. Introduction

Eruption dynamics are assumed to be controlled mainly by the composition and physical properties of magma (Cassidy et al., 2018; Sparks, 1978; Wilson et al., 1980). They determine the amount of gases that magma may dissolve, the rate at which these gases will separate from magma when approaching to the surface and, consequently, whether the eruption will be mainly effusive or explosive. Totally effusive or explosive volcanic eruptions are not rare, but eruptions alternating between the two types of activity, or showing a complete gradation from highly explosive to highly effusive, are even more common and may indeed occur for all magma compositions. The causes that determine these changes in eruption dynamics have already been the subject of many studies. Different factors have been proposed to explain such evolution, including changes in magma degassing that occur both prior to and during the eruptions, variations in magma permeability, and differences in conduit properties (e.g. Cashman, 2004; Cassidy et al., 2018; Degruyter et al., 2012; Eichelberger et al., 1986; Gonnermann and Manga, 2003; Lavallée et al., 2015; Woods and Koyaguchi, 1994).

Teide and Pico Viejo (T-PV) stratovolcanoes, on the island of Tenerife (Canary Islands), have alternating effusive and explosive activities that show both abrupt and gradual transitions among them during their phonolitic period, which covers the last 30 ka (Ablay and Martí, 2000; Martí et al., 2008). This phonolitic activity has been mostly central, but also includes numerous satellite flank eruptions with both effusive and explosive phases, which

are characterised by the construction of large dome-like structures. In calc-alkaline magmas, such an occurrence of effusive and explosive phases in dome-forming eruptions is common, having been described for many volcanoes (e.g., Boudon et al., 2015; Lavallée et al., 2015; Martel et al., 2000; Nakada et al., 1995; Sparks, 1997). However, in the case of T-PV, dome formation shows an atypical pattern compared to classical calc-alkaline counterparts, as the lava domes correspond to the product of syn-depositional agglutination from spattering activity (e.g., Ablay et al., 1995; Andújar and Scaillet, 2012a and b), rather than a protrusion resulting from the slow extrusion of viscous lava.

Despite the fact that most historical volcanism on Tenerife has been related to basaltic magmas and has occurred outside T-PV stratovolcanoes, these should be considered active volcanoes, being able to produce new eruptions in the near future (Martí et al., 2008). Hence, understanding the causes and characteristics of satellite dome eruptions is vital to correctly interpret monitoring data and conduct a precise hazard assessment.

In this study we contribute to the understanding of the mechanisms that control a characteristic dome-forming eruption at Teide volcano in which a progressive change in the style of activity has occurred from an efficiently fragmented magma dispersed by a sustained plume to a poorly-fragmented low-height, non-convective fountain (forming a fountain-fed lava dome) to a glass-bearing lava flow. We describe the petrology and geochemistry of the Pico Cabras dome-forming eruptive products to determine their pre-eruptive parameters and to thereby propose a conceptual model for the magmatic reservoir prior to eruption.

2. Geological background

T-PV stratovolcanoes started to grow simultaneously at about 180 ka ago within the Las Cañadas caldera (Fig. 1), a volcanic depression formed by several vertical collapses of the former Tenerife central volcanic edifice (Las Cañadas edifice), following explosive

emptying of a shallow magma chamber. Several large scale, lateral collapses of the volcano flanks also occurred, modifying some sectors of the resulting caldera depression (Martí, 2019; Martí and Gudmundsson, 2000).

Eruptions at T-PV have evolved compositionally from basanitic to phonolitic and have occurred from both their central vents and from a multitude of satellite vents distributed on their flanks. Felsic products, however, dominate the recent output of the T-PV system and represent 83% of the total volume emitted during the last < 30 ka (Ablay and Martí, 2000; Martí et al., 2008).

The eruptive style of T-PV phonolitic eruptions depends on vent location (central or lateral). In central eruptions (with origins in T-PV main craters) the eruptive style has been dominated by effusive to transient explosive eruptions, with ash columns of up to a few kilometres and the production of scoria and spatter deposits, together with lava flows (Ablay and Martí, 2000; Martí et al., 2008). Meanwhile, satellite vents are characterised by the highest explosivity and the generation of major ash columns, the collapse of which produced important fallout and PDCs deposits. Some of these satellite eruptions (e.g., Montaña Blanca and El Boquerón) have been classified as sub-plinian to plinian eruptions (Ablay et al., 1995; Andújar & Scaillet, 2012b; García et al., 2012). Furthermore, these lateral eruptions are characterised by the formation of a typical dome-like structure constructed on the vent by agglutination of large spatter clasts, at the same time or preceding the emplacement of clastogenic, glassy lava flows (e.g., Ablay et al., 1995).

Pico Cabras dome is approximately 600 m long, 450 m wide and has a height of 130 m (Fig. 2). Based on its stratigraphic position, its age has been placed between 9210 and 5911 years BP (Ablay & Martí, 2000; Carracedo et al., 2007). The deposits of this eruption are well preserved in the geological record and show a progressive gradation from highly explosive to poorly or non-explosive activity.

3. Field characteristics of Pico Cabras deposits

The Pico Cabras succession includes at its base, a pumice fall deposit, which is partially reworked and eroded out, from a few centimetres to a maximum of 2 m thick, formed of angular to sub-rounded lapilli pumices. It occurs in a few well-preserved outcrops composed of well-sorted, greenish to grey, poorly vesiculated pumices, with a few obsidian lithic fragments (3-4% vol.), showing well-defined stratification. However, there are no stratigraphic indicators that could be used to correlate individual layers among the different outcrops, so the Pico Cabras pumice deposit has been therefore characterised as a single unit (García et al., 2014). The basal contact of the pumice deposit with previous lavas is not well exposed; upwards it grades into agglutinated spatter deposits that form the dome structure. This transition is only visible at certain points around the dome while in most places the pumice fallout is covered by the rheomorphic welded spatter (Fig. 2).

The dome shows an internal clastogenic appearance, similar to most of the T-PV domes (e.g., Ablay et al., 1995), also showing the piling up of different units of strongly welded spatter clasts, ranging in size from a few centimetres to several decimetres. They behaved rheomorphically forming short lava-like lobes in all directions from the dome centre.

Pico Cabras also emitted several lava flows, with a total volume of 0.28 km3 DRE (Dense-Rock-Equivalent). They all flowed down through a narrow channel at the centre of the dome towards the north of the island. All these lavas are glassy and autobrecciated forming large irregular blocs in a chaotic distribution. Compared to the spatter clasts of the dome, the obsidianic lavas look very fresh.

4. Methodology

Representative samples from Pico Cabras deposits, from the sub-plinian fallout (including spatter fragments) and the lava flows, were collected for further mineralogical and geochemical characterisation. The crystal content of the samples was obtained by the point counting method on respective thin sections and, in the case of the pumice samples, from separate minerals. Owing to the low amounts of phenocrysts present in the pumice samples (less than 0.5%), different fall-out pieces were crushed and sieved until obtaining a coarse-grained powder, from which several minerals and glass fragments were hand-picked in order to proceed with their observation under different microscope techniques.

The samples were analysed with a Scanning Electron Microscope (SEM) Merlin Compact ZEISS with an EDS Bruker detector (QUANTAX-XFlash6) at the Institut des Science de la Terre d'Orleans (ISTO, Centre National de la Recherche Scientifique, Orléans, France). Additionally, we performed a micro-X-Ray Fluorescence (Micro-XRF) analysis using the XTRACE detector (Tube Rh - filters Al, Ti, and Ni) connected to the SEM, which was calibrated against inner Br glassy standards containing different amounts of Br (Faranda et al., 2019) in order to analyse Br in sodalite and glass in the pumice samples. Mineral phases and glass compositions were obtained with an electron microprobe SX-FIVE, also installed at ISTO. An acceleration voltage of 15 kV, a sample current of 6 nA, and a counting time of 10 s were used. Na and K were analysed first and a ZAF correction procedure was applied if necessary. Major elements calibration was performed using standards of: albite (Na, Si), orthoclase (K), andradite (Ca), topaz (F), apatite (P), vanadinite (Cl), baryte (S), corundum (Al), magnesium oxide (Mg), nickel oxide (Ni), hematite (Fe) and pyrophanite (Mn, Ti). For the oxides, the relative analytical errors are 1% (SiO_2, Al_2O_3, CaO), 3% (FeO, MgO, TiO_2) and 5% (MnO, Na_2O, K_2O, P_2O_5). For the glasses, a large defocused beam of 10x10 or 20x20 μm was used to minimise alkali-migration during their analysis, whereas for minerals a focused beam was employed. In this work, total iron content is noted as FeO*.

Whole-rock data was obtained by analysing two glass samples resulting from the two-step melting (with grinding in between) of lava and pumice samples at 1400 ºC for 4 hours in total time, respectively.

As a way to make the results of this work accessible to the scientific community, all the research data obtained is available at the open-access repository DIGITAL.CSIC (http://digital.csic.es/) as Dorado et al. (2020) with DOI http://dx.doi.org/10.20350/digitalCSIC/12715, and also in the Supplementary Material. The four samples used in this work have been registered in the online System for Earth Sample Registration database (http://www.geosamples.org): three of them (IEODG0001, IEODG0002, and IEODG0004) are samples from the lava flow and the remaining one (IEODG0003) is made up of pumices from a lapilli level.

In order to constrain the pre-eruptive parameters of the magmas related to the different phases, we used available phonolitic-melt thermometry (Martí et al., 2020), the clinopyroxene-liquid barometric and thermometric equations of Masotta et al. (2013) and the K-feldespar-liquid hygrometer of Mollo et al. (2015), since these were previously calibrated on magmas from Tenerife that were compositionally similar to those emitted from Pico Cabras. These models back-calculate the above parameters with a precision of ± 16-18 ºC for T; ± 0.75 wt.% for H_2O melt contents, and ± 120 MPa for P, respectively.

5. Results

5.1. Petrography

5.1.1. Pico Cabras pumices

Representative pumices examined in this work are sub-rounded, greenish to gray lapilli fragments, with an average size of ~1-2 cm. They are microvesicular, glassy, phonolitic in composition, and crystal poor (with a maximum of 0.5% crystal content). The

mineral assemblage found in the pumices includes feldspar (fsp), clinopyroxene (cpx), biotite (bt), magnetite (mt), ilmenite (ilm), apatite (ap), and traces of sodalite (sdl) (Fig. 3). A few titanite crystals, associated with clinopyroxene and magnetite, were also identified. Moreover, spatter clasts were also sampled but they were not useful to this analysis as all them were formed of totally aphyric, partially devitrified obsidian, occasionally showing surface microliths formed during cooling.

Feldspar and biotite are the most abundant and largest phenocrysts (between 0.5 and 1.5 mm). They are mostly euhedral, but some slightly rounded biotite crystals were also found (Fig. 3g). Clinopyroxene, magnetite and ilmenite are usually found as aggregates, however with smaller sizes (maximum of 0.5 mm) when compared to previous ones. Apatites of pumice and lava flow products currently appear as inclusions within other minerals (i.e., clinopyroxene, biotite, or magnetite (Fig. 3).

In addition, it is also remarkable to observe the presence of sparse, small (1 mm) crystals of sodalite (Cl-rich feldspathoid), which present rounded edges, numerous fluid inclusions and, to a lesser extent, glass inclusions (Fig. 3h). They also have small iron sulphide (pyrite or pyrrhotite) crystals inside, whose exact identification was not possible due to their small size. Along with Beard et al. (2019), this is the second time that sodalite is reported in the most recent phonolites from Teide. This low-abundant mineral, however, also appears frequently in previous deposits from the Las Cañadas edifice (< 180 ka; Araña and Brändle, 1969; Bryan et al., 2002; Martí et al., 2020; Wolff and Storey, 1984).

Phenocrysts are set in a microvesiculated phonolitic glassy matrix containing less than 0.1% Fe-Ti oxide, biotite, clinopyroxene, and alkaline feldspar.

5.1.2. Pico Cabras lavas

The studied lava products have porphyric texture and a phenocryst content of ~5%. Feldspars from 0.5 to 5 mm in length dominate the mineral assemblage, together with lesser

amounts of diopside (sizes from 0.1 to 1.5 mm), biotite (from 0.1 to 0.5 mm), magnetite and ilmenite (from 0.1 to 0.4 mm), as well as small apatite crystals. The groundmass is also phonolitic with glass feldspar microlites and, to a lesser extent, tiny crystals of clinopyroxene, biotite, magnetite, and ilmenite (Figs. 3a-f).

Lava feldspars are subhedral to anhedral, prismatic phenocrysts with (Fig. 3a, d) some displaying partially rounded and reabsorbed rims. They can also contain inclusions of smaller mineral phases such as biotite, clinopyroxene, Fe-Ti oxide, and apatite (Fig. 3a).

The rest of the mineral assemblage (cpx-bt-mt-ilm-ap) appear as both isolated phenocrysts or within agglomerates (Fig. 3b). Biotite and clinopyroxene are often euhedral to subhedral, however, rare crystals with completely rounded edges are also present in the samples (Fig. 3e). Frequently, magnetite and ilmenite appear together, with subhedral to euhedral shapes, indicating cosaturation. One feature common to all magnetites is the presence of ilmenite exsolution lamellae within the phenocrysts forming grids smaller than 1 μm in thickness, which suggest sub-solidus re-equilibration of these phases during ascent, or after emplacement (Lattard, 1995; Fig. 3c). It is also remarkable to observe the presence of just one amphibole (kaersutite) crystal in Pico Cabras phonolite lavas (Fig. 3f), whose external origin will be discussed later based on chemical composition and calculated mineral-glass K_D.

5.2. Mineral chemistry

5.2.1. Feldspars

Analysed feldspars from the studied samples when plotted in the Orthoclase (Or)-Albite (Ab)-Anorthite (An) classification diagram (Fig. 4; Deer et al., 1972) show a continuous evolutionary line from anorthoclase-oligoclase type to sanidine feldspars ($Ab_{74}Or_{12}An_{14}$ to $Ab_{54}Or_{44}An_{2}$), encompassing the lineages defined for the actual T-PV system (Ablay et al. 1998; Triebold et al. 2006). Several distinct feldspar populations have

been found within the different eruptive phases, as well as different zoning trends (Figs. 5 and 6; Table 1).

All feldspar cores found in the lava flow are anorthoclase with compositions being in the range An_{4-7} (Figs. 4 and 5). Despite the subtle differences, population histograms and EMPA compositional profiles reveal the presence of a dominant groups at $Ab_{68-70}Or_{23-25}An_{6-7}$ and a less frequent but also important one at $Ab_{67}Or_{29}An_{4-5}$ (Figs. 5, 6a; Table 1). Compositional profiles performed on feldspar crystals (Fig. 6a, 6b) also allowed us to identify the presence of rims (~50 µm in size) having two distinct compositions. The first rim type is characterised by an enrichment in An and FeO* content ($Ab_{65-69}Or_{22-26}An_{9-10;}$ 8-10 wt.% FeO*) compared to the cores (Fig. 6a) and the second shows a depletion in these two elements ($Ab_{64}Or_{35}An_{2}$) in comparison to crystal centres (Figs. 6b, c; Table 1).

Meanwhile, feldspar cores in the pumices show a much larger variation and can be divided into two distinct populations (Fig. 5; Table 1). The compositional range of the first group coincides with the cores found in the lavas ($Ab_{67-70}Or_{25-28}An_{4-7}$) and are also classified as anorthoclases (Fig. 4). The second group, in contrast, have relatively low An contents ($Ab_{57-64}Or_{35-42}An_{0-1.5}$) compared to the former ones and can be classified as much more evolved anorthoclases and sanidines as shown by Ablay et al. (1998) and Andújar et al. (2008). Some of them also present relatively wide variations in Ab and Or content within the same crystal (up to 5 mol.% in several crystals). Only one zoning trend has been found in this second group, with a rim composition of $Ab_{61}Or_{38}An_{1}$, which is common in cores from the two populations (Figs. 5 and 6c).

The genetic relationship between the different feldspar phenocryst populations from Pico Cabras products is also supported by the trend described in Figure 7, which plots FeO* content in feldspars versus log (Or/An). This parameter works as a fractionation index and a proxy for identifying the degree of differentiation of the magma from which the minerals

have crystallised (Triebold et al., 2006). Feldspars from the pumices are the ones that present a higher degree of differentiation (log Or/An between 1.4 and 2.5), except the group that coincides in composition with the phenocrysts found in the lava flow (values between 0.5 and 0.8). Rims depart slightly from these values, both towards more evolved or more mafic compositions.

Microlites analysed from both lava flow and pumices show a large chemical variation that overprint the evolutionary line described by the cores, from anorthoclase-oligoclase to sanidine (from $Ab_{74}Or_{12}An_{14}$ to $Ab_{58}Or_{38}An_4$) (Fig 4 and 5; Table 1). This large variation occurs even within the same sample for nearby microlites. Some of the microlites enriched in An are also enriched in iron (up to 1.4 wt.% FeO*) compared to most of the feldspar analysed (average of 0.28 wt.% FeO* in the lava flow and 0.23 wt.% FeO* in the pumices). The huge variation in microlite composition is also represented in Figure 7, with some of them reaching values typical from intermediate magmas (log(Or/An) values close to zero or even negative, with high FeO* contents).

5.2.2. Clinopyroxenes

Clinopyroxenes from Pico Cabras can be classified mainly as diopside according to the classification of Morimoto (1988), with only one core from a pumice clast presenting augite composition (Fig. 8a, Table 2).

Clinopyroxene phenocrysts found in the lava flow present a fairly homogeneous composition at $Wo_{46-48}En_{38-41}Fs_{12-16}$ with Mg# between 71 and 77 (where Mg# $=X_{MgO}/(X_{MgO}+X_{FeO*})x100$, and X_i is the mole fraction of i in the liquid) without core-rim zoning. In comparison, the phenocrysts found in the pumices are slightly more evolved ($Wo_{43-47}En_{29-38}Fs_{15-28}$; Mg# from 51 to 71) and contain somewhat lower Al_2O_3 (0.4 wt.%) and TiO_2 (0.2 wt.%) compared to the former ones.

Only one analysed crystal from the explosive products shows core-to-rim variation, with a Fe-rich core ($Wo_{43}En_{29}Fs_{28}$) and a Mg-rich rim ($Wo_{46}En_{33}Fs_{21}$). This more evolved core is also enriched in Na (up to 3.2 wt.%) and Mn (up to 1.5 wt.%) (Table 2).

5.2.3. Biotite

Analysed biotites are all MgO- and TiO_2-rich, with Mg# ranging from 57 to 67 (calculated as for clinopyroxene). They exhibit an SiO_2 content from 35 to 39 wt.%, Al_2O_3 from 12.3 to 16.6 wt.%, K_2O from 8.1 to 9.2 wt.% and TiO_2 from 6.8 to 8.4 wt.% (Fig. 9; Table 3). Biotites from the lava flow have higher Mg# (average of 65) values than those in the pumices (average of 63). This last group is also the only one showing moderate chemical variation within the crystals, with rims having lower Mg# (between 56 and 61), Na_2O, K_2O (~0.3 wt.%) and higher SiO_2, Al_2O_3 and MnO contents (up to 2 and 0.3 wt.% respectively) compared to the cores.

5.2.4. Amphibole

One subhedral kaersutite amphibole crystal was found in the Pico Cabras lava flow close to a biotite and separated by a reaction rim. As amphibole is not a common phenocryst that crystallises from evolved phonolitic magmas at T-PV (Andújar et al., 2008; 2013), we used the Putirka (2016) crystal-liquid distribution coefficients (K_D) to find out if both magma and amphibole were in equilibrium. The calculated kaersutite-melt for this crystal (K_D) falls out of the equilibrium range values (equilibrium $K_D Fe\text{-}Mg^{Amp\text{-}liq}$ between 0.077 and 0.117) determined by Putirka (2016), which testifies for the xenocrystic origin of this mineral.

5.2.5. Iron-titanium oxide

The iron and titanium oxides fall within the compositional series of T-PV magnetite and ilmenite (Ablay et al., 1998; Andújar et al., 2008; 2013). Magnetite phenocrysts always present tiny ilmenite exsolution lamellae (Fig. 3c). This feature made it difficult to obtain precise compositional results, with values ranging from Ilm_{87} to Ilm_6 (the latter from a

magnetite rim present in an ilmenite phenocryst without exsolutions). In contrast, ilmenite phenocrysts display more homogeneous values (between Ilm_{70} and Ilm_{100}) due to the lack of exsolutions (Table 3). Based on textural observations, magnetite and ilmenite cosaturate from the melt.

5.2.6. Sodalite

Sparse sodalite crystals were found in the pumices from the explosive phase, with a homogeneous composition (Table 3). Small iron sulphide crystals were found within the sodalite as inclusion bands (reaching a FeO^*+SO_3 content of up to 1.6 wt.% in those zones), textures which are similar to those identified in haüynes from pre-Teide evolved phonolites (Cooper et al., 2015) and some fluid and melt inclusions which were not analysed in this work. A mean of 130 ± 13 ppm of bromine was measured inside the crystal using micro-XRF analysis.

5.3. Whole-rock and residual glass

EMPA data from pumices and lava flow representative glasses (resulting from the complete melting of the samples -see above) indicate that all the products are phonolitic in composition (Le Bas et al., 1986) with some products straddling the trachyte-phonolite border (Fig. 10; Table 4). The only observable difference between the two phases is found in the TiO_2 content, where the lava sample is slightly enriched (up to 1.2 wt.%) compared to the pumice sample (up to 0.8 wt.%).

Residual glasses are also phonolites (Fig. 10; Table 4) (Le Bas et al., 1986), the whole set of data displays a continuous liquid line of descent, with SiO_2 depletion along with alkali enrichment (Ablay et al., 1998, Wolff, 1987; Wolff and Toney, 1993). The less evolved liquid corresponds to the bulk lava composition and the most evolved corresponds to the residual matrix glass found in crystal-rich lava (Table 4).

Residual glass from pumice samples plots on the differentiation lineage defined by previous products being this way, however, slightly depleted in SiO_2 and CaO and enriched in Na_2O compared to the whole-rock (Figs. 10; Table 4). Additionally, we analysed the amount of halogen volatiles (Cl, Br, and F) present in the glasses. Cl varied between 0.2 and 0.6 wt.% and F from ~0 up to 0.3 wt.% in the phonolitic glasses. The XRF analysis of Br yielded concentrations of 10 to 15 ppm.

5.4. Pre-eruptive parameters: P, T and H_2O

The first estimates concerning pre-eruptive temperature were obtained by applying the new empirical and experimentally-derived geothermometer for phonolitic melts from Martí et al. (2020) to the different melts analysed in this work (whole rock (WR) lava, WR pumice, residual matrix pumice and lava; Table 4). We should consider that applying this geothermometer to phonolites with a significant number of crystals (i.e., residual melts with compositions significantly different from those corresponding to the whole rock) may provide inaccurate results (Martí et al., 2020). Thus, for retrieving temperatures with this model we considered the bulk melted and residual glass compositions analysed for the fall-out products and the composition of the full melted glass for the lava, since for this last one the glassy groundmass experienced profuse syn-eruptive crystallisation and therefore do not match the utilisation criteria provided by the authors. This empirical equation back-calculates T with an uncertainty of ± 16 ºC.

The calculations yield average temperatures of 867 ± 23 ºC and 842 ± 19 ºC for the bulk and residual glass of the fall-out and 902 ± 24 ºC for the whole rock lava. Errors on calculated temperatures consider both the standard deviation of the average calculated T and the model uncertainty. Comparatively, the probability distribution analyses of the calculated temperatures point towards somewhat lower values (7-12 ºC) compared to the average,

however such differences are smaller than the uncertainty associated with the calculations (Fig. 11a). These results are in good agreement with those determined for similar Teide phonolites (Ablay et al., 1995, 1998; Andújar and Scaillet, 2012b; Andújar et al., 2010, 2013; Wolff 1985).

Water contents dissolved in magma were calculated using the alkali feldspar-melt hygrometer of Mollo et al. (2015). The inputs for the model were the alkali feldspar-melt compositions of the Pico Cabras products and the temperatures obtained from Martí et al. (2020). To make sure that the considered alkali-feldspar-melt pair was in equilibrium, we used the test based on feldspar-melt exchange reactions [$K_{D(Or\text{-}An)}^{kfs\text{-}liq}$] proposed in Mollo et al. (2015). The compositions plotted within 10% of the one-to-one line between the predicted K_D and the measured K_D are considered to be in equilibrium. According to the authors (Mollo et al., 2015), a margin of error of ± 0.75 wt.% is normally associated with the magma water content estimated using this method. However, when the errors of the above calculated temperatures are also considered, the accuracy on water-determination increases to ± 0.9 wt.%.

Unfortunately, only 42 of 217 pairs tested in the model were in equilibrium. In general, all feldspars with anorthite contents exceeding 5 mol.% (phenocrysts from lava, pumices and microlites) were out of the accepted range (Fig. 12; Appendix A). In contrast, the population with An ≤ 5 mol.% from both fall-out and lava products, passed the equilibrium test. Regardless, we decided to present the results here. The applicability of the results and the use of this method with this type of magma will be discussed later in this article.

For the lava flow, water contents retrieved for feldspars accomplishing the equilibrium requirements ($An_{2\text{-}4}$) yield average water contents of 4.5 ± 0.9 wt.% (standard deviation, σ = 0.42, number of calculations, n = 5), which match the maximum probability

peak. In contrast, the An-rich crystals and rims (An_{7-10}; not in equilibrium) yield lower H_2O contents from 3.5 down to 2.9 ± 0.9 wt.% (Figs. 11b, 12).

For the pumices, the distribution of probabilities shows the existence of two well distinct populations depending on their An content (Figs. 11b, 12). Those with An_{4-5} yield relatively similar water contents of ~ 4.5 ± 0.9 wt.%, values that are in close agreement with the ones retrieved for the same K-feldspar population present in the lava flow. In contrast, Ca-poor crystals (An ≤ 1.5 mol.%) back-calculated a large range of H_2O, from 4.5 to up to 7 wt.%; most of the population being at ~ 6 ± 0.9 wt.%, contents that are somewhat higher than the calculated average (5.2 ± 0.9 wt.% H_2O, σ = 0.86, n = 29).

Quantitative pressure and temperature estimates were also obtained using the clinopyroxene-liquid P-independent geothermometer (Eq. Talk2012) and T-independent geobarometer (Eq. Palk2012) of Masotta et al. (2013). According to the authors, these equations have a standard error of the estimate (SEE) of ± 18 ºC and ± 120 MPa, respectively. In this case, when the uncertainty of above calculated H_2O contents and the standard deviation of the different bulk compositions are considered, the retrieved P and T are impacted by ± 10 MPa and 5 ºC respectively. This yields total uncertainties of ± 130 MPa and ± 23ºC for the retrieved P-T.

As a test for equilibrium, this geothermobarometer uses the T-sensitive model for Fe-Mg exchange [$K_D(Fe\text{-}Mg)^{cpx\text{-}liq}$] of Putirka (2008). In our calculations we only considered clinopyroxene-liquid pairs with $K_D(Fe\text{-}Mg)^{cpx\text{-}liq}$ values between 0.09 to 0.37, which according to the authors, are in equilibrium (Masotta et al., 2013). Additionally, we assumed the previous calculated average melt-water contents of 4.5 wt.% in the effusive phase and 5.2 wt.% in the explosive phase.

The application of the Masotta et al. (2013) parameterisation on lava flow clinopyroxene phenocrysts yield temperatures between 884 and 911 ºC, with an average

value of 898 ± 23 ºC (σ = 7.8, n = 15; Fig. 11c). These in turn returned crystallization pressures between 60 and 140 MPa, with only an extremely high value at 290 MPa (Fig. 11d). The average P of the effusive cpx dataset is 110 ± 130 MPa (σ = 0.55, n = 15), a somewhat higher value compared to the position of the dominant probability distribution peak at 80 ± 130 MPa. For pumices, the obtained temperatures are somewhat lower (846-880 ºC) compared to the lavas, with an average value of 863 ± 23 ºC (σ = 9.6, n = 17). For pressures, these show a continuous distribution from 90 to 340 MPa, with an average P at 180 ± 130 MPa (σ = 0.64, n = 17). This last one matches the top of the probability distribution poorly defined region fairly well at 170 ± 130 MPa (Fig. 11d).

According to these estimates two different magmas would have been present in Pico Cabras eruption. The lava flows of this eruption would have tapped a magma ponded at ~900 ºC, containing 4.5 wt.% H_2O and located at a depth of 0.5-1.5 km b.s.l (below sea level) (~100 MPa). Whereas in turn, the pumices would have been related to a somewhat cooler (~865 ºC), water-rich (~5-7 wt.% H_2O) but deeper body ponding at 170 MPa (~2.5 km b.s.l). These conditions are consistent (considering errors) with the melt thermometry estimates and those experimentally determined for similar Teide-Pico Viejo phonolitic products (Andújar and Scaillet, 2012b; Andújar et al., 2010, 2013). However, when the uncertainties associated with each calculated parameter are considered, which are especially high for P (± 130 MPa), the storage conditions overlap to a high extent (Fig. 13). Thus, in the next section we integrate the stratigraphic information, eruptive sequence, mineral compositions and zoning along with existing phase equilibria studies to discriminate between the following scenarios: a single reservoir being thermally, compositionally and volatile-zoned versus two different magma bodies that interacted prior to the eruption.

6. **Discussion**

6.1. Refining pre-eruptive conditions by comparison with phase equilibrium results.

In the case of the Pico Cabras eruption, pre-eruptive parameters estimated by different geothermobarometers and the geohygrometer show significant differences between the distinctive products of the eruption (Figs. 11 and 13), especially with regard to temperature and, to a lesser degree, H_2O and pressure. To provide tighter constraints, here we refine the above estimates by comparing the petrology of the natural phonolites to the information gained in experimental works that were performed on similar phonolitic compositions. Compared to other methods (i.e., statistical studies), phase equilibrium experiments can provide first-order constraints under magma pre-eruptive conditions since these are powerful tools to simulate realistic magmatic conditions and explore the sensitivity of mineral stability and composition to changes in the intensive parameters (Martel et al., 2017).

Magma corresponding to the lava flows shows higher temperatures: average of 902 ºC and 898 ºC with the calculations of Martel et al. (2020) and Masotta et al. (2013) (SEE of ± 16 ºC and ± 23 ºC, respectively). On the other hand, it presents lower pre-eruptive water content (average of 4.5 wt.%)

The lava samples present a mineral assemblage consisting of ~5% alkali feldspar, magnetite, ilmenite, clinopyroxene, and biotite. This low crystallinity and paragenesis is well reproduced in experiments between 50 and 100 MPa, 850-900 ºC and H_2O contents between 3-4.5 wt.% (Andújar and Scaillet, 2012b; Andújar et al. 2013). The absence of titanite also suggests T > 850 ºC, since this phase is always present at lower temperatures in these magmas (Andújar and Scaillet, 2012b). These conditions correspond to the ones obtained here using the available geothermobarometer and geohygrometer, with the only exception being one analysis that yielded a value of 280 MPa. However, this is a non-realistic value for this magma, since at such a pressure and considering the previous T-H_2O contents, the crystal-cargo would exceed 15% (Andújar and Scaillet, 2012b; Andújar et al. 2013).

Mineral chemistry also confirms this first estimate: the two feldspar core populations ($Ab_{68-70}Or_{23-25}An_7$ and $Ab_{67}Or_{29}An_4$) were closely reproduced experimentally at 900 ºC and 850 ºC respectively (Andújar et al., 2008, 2013). So, we consider the average temperature of the magma for the Pico Cabras lava to be 880 ± 30 ºC, with slight temperature variations within the chamber (see below). On the other hand, the same experiments reproduced feldspar rim populations and microlites ($Ab_{65-69}Or_{22-26}An_{9-19}$ and $Ab_{64}Or_{35}An_{1.5}$) at 950 ºC and 825 ºC, respectively. At this temperature, the lowest crystallinity (5-10%) is found in experiments at 100 MPa and 2.5-3 wt.% H_2O (1-2 wt.% below the ranges estimated by the geohygrometer).

Natural biotites are also well reproduced under the conditions stated above. In terms of clinopyroxenes, the analysed compositions slightly differ from the experiments: they have a little higher enstatite content (from 38 to 41 mol%) and Mg# (from 72.5 to 76.5). This can be explained by higher temperatures (900-950 ºC), in line with the most An-rich feldspars.

Concerning pumices, storage conditions retrieved by empirical equations span a large range of pressures (90-340 MPa), water contents (4.5-7 wt.%) and temperatures (842-880 ºC). Compared to the lavas, the crystallinity of the phonolitic pumices is significantly lower and the paragenesis contains sodalite, titanite, and some mineral compositions that were not identified in the former (feldspars with An ≤ 1.5 mol.%).

In terms of bulk-rock composition and, specially, mineralogy, pumice products share some similarities with those of the El Abrigo eruption (Andújar et al., 2008), which was the last caldera-forming eruption from Las Cañadas Edifice, occurring about 180 kyr. ago (Martí et al., 1994). The most notable difference between these two magmas is that El Abrigo carries haüyne instead of sodalite, otherwise the paragenesis is almost the same. Haüyne and sodalite are present in trace amounts in phonolites and share a similar P-stability dependence on phonolitic melts (Andújar et al., 2008; Berndt et al., 2001; Wellmann, 1970). According to

these works, the presence of these phases in the magma sets a maximun pressure limit at 125-170 MPa, the variation on the H2O-content havinga limited impact on it (±25 MPa)

In this case, the coexistence of all the phases of the mineral assemblage can be only possible at T < 850 ºC; P < 150 MPa, and H_2O < 5 wt.%., as at higher P-T-H_2O, the magma will never crystallize feldspar and the paragenesis would be hence dominated by mt+bt or mt+bt+cpx+tit (Andújar et al. 2008). This observation indicates that the extreme water content values we obtained using the Mollo et al. (2015) geohygrometer (H_2O > 5 wt.%) are not realistic for this magma.

Thus, to refine our previous estimates we use the composition of the mineral phases present in the pumices. Feldspars found in the Pico Cabras pumices, as mentioned in previous sections, can be divided into two distinguishable populations. The first is similar to the ones found in the lava flow ($Ab_{67-70}Or_{25-28}An_{4-7}$), while the second is much poorer in anorthite ($Ab_{57-64}Or_{35-42}An_{0.5-1.5}$). The latter is closely reproduced at temperatures between 725 and 825 ºC, 100 MPa and 3-4.9 wt.% H_2O (Andújar et al., 2008, 2013). However, when considering the sample crystallinity (< 1%) only the experiments at 725 ºC successfully reproduce feldspars with that composition (An < 1.5 mol.%). The An-rich population, on the other hand, would have crystallised under conditions similar to those described for the lava flow (880 ± 30 ºC; see above).

Under these conditions, natural biotites are also well reproduced: cores (Mg# between 61-65) at 100 MPa, 800 ºC, and 4 wt.% H_2O; and rims (Mg# between 56 and 61) with temperatures below 800 ºC. Clinopyroxenes crystallised at 100 MPa and ~825 ºC closely reproduce the Fs-rich phenocrysts in pumices ($Wo_{43}En_{29}Fs_{28}$). En-rich cores and rims ($Wo_{46}En_{33}Fs_{21}$) are also well reproduced with the P-T-H_2O conditions we constrained for the lavas.

One point that requires special attention is the presence of highly evolved sanidines (An ≤ 1.5) and iron-rich clinopyroxenes in the pumices, which, according to our previous estimates, could both not directly crystallise from the magma compositions sampled in this work, nor at the P-T-H_2O values previously determined for both of the magmas. However, the highly evolved character of these phases compared to those predominating in the lavas suggests that the former crystallised from a more evolved phonolitic melt. The comparison with available experimental data confirms that the potential parental magma producing such pumices phenocrysts has a composition similar or equivalent to that of the El Abrigo magma (Andújar et al., 2008). If this magma was stored at 725 °C and contained a higher water content (3.5-5 wt.%), the crystallisation of these highly evolved mineral phases from an El Abrigo equivalent magma could be possible. Further evidence is provided by the subtle differentiation trend described by residual glasses from the pumices. The most evolved compositions of this series have total alkali and SiO_2 contents that are identical to those of El Abrigo (Fig.10).

6.2. Structure of the Pico Cabras reservoir prior to the eruption

The comparison of the petrological information with experimental data allowed us to refine the estimates provided by the empirical methods. In summary, both magmas were stored at ~100 MPa (± 50 MPa) and contained slightly different water contents (3 wt.% for the lavas and 5 wt.% for the pumices) but showed very different temperatures, these being in the range 725-825 ºC and 850-900 ºC for the pumices and the lavas, respectively. This points towards the existence of a unique reservoir where magmas co-existed prior to the eruption. Field evidence along with the petrology of the natural samples further support such a scenario. The lack of An-poor feldspar crystals ($An_{<1.5}$) or other evolved mineral phases like the ones found in the pumices within the lavas deposits, rules out the unlikely situation where

the most evolved magma rising from deeper levels interacts and passes through the most mafic and shallower one, as suggested by cpx-geobarometry (Fig. 13). Additionally, in the case studied here, the emplacement of pumices precedes that of the lavas, the former not showing evidence of long-term chemical interaction (e.g., reverse zoning in sanidines $An_{1.5}$ to An_4) with its more mafic counterpart.

By integrating this information, we are able to propose the following conceptual model to explain the Pico Cabras dome-forming eruption. The phonolitic reservoir that fed Pico Cabras eruption was located at a pressure of about 100 ± 50 MPa (around 1 km b.s.l). This was chemically, thermally, and volatile-zoned prior to the eruption (Fig. 14). The main body of the reservoir was formed by a phonolitic magma being at temperatures of 880 ± 30 ºC and containing 2.5-3 wt.% dissolved H_2O. Least squares mass-balance calculations relate the lava and pumice WR compositions by the crystallization of 0.8 wt.% of Fe-Ti oxides, 0.1 wt. % Bt, 0.5 wt. % Cpx and 3.9 wt. % of An_4 K-feldspar ($\Sigma R^2 = 0.08$). Since, these mineral proportions are similar to those determined for the phonolite lavas, we can confirm that the uppermost part of the reservoir hosted the residual melt derived from the crystallization of the former one, it being cooler (725-825 ºC) and containing a higher water content (3-5 wt.%) than the main magma. At these pressures, the estimated water contents are slightly far from saturation (5-6 wt.% H_2O at 100-150 MPa, respectively; Schmidt and Behrens, 2008), an observation that supports the general water-undersaturated character of Tenerife phonolites (Andújar and Scaillet, 2012a). Other volatiles (S, Cl, Br) were also present in this upper part. However, our results cannot assess the co-existence of an independent fluid-phase containing an excess of these minor gas-phases (i.e., brine-rich fluid phase, Bureau et al., 2000; Signorelli and Carroll, 2000) with the Pico Cabras magmas.

Eruption started with the explosive emission of the uppermost magma, forming a sub-plinian eruption column, which rapidly waned in intensity given rise to a low fire fountaining

eruptive phase of hotter and less volatile-rich magma. Hot, large scoria fragments accumulated and agglutinated on the vent, experiencing rheomorphism and forming the dome-like structure. The last part of the eruption corresponded to the emission of the main part of the chamber in the form voluminous obsidianic lava flows that branched at the southern side of the dome. The profuse surface crystallization of feldspar microlites, clinopyroxene and Fe-Ti oxides in the lava during its downward flow (see above), generated the highly Na-rich residual melts measured in this work. In essence, this eruption sequence reflects the eruption of progressively hotter and less volatile-rich phonolitic magmas, without any other clear interference of internal or external factors (e.g., final mingling, variation in conduit size). The progressive change in the style of activity, from an efficiently fragmented magma to a poorly-fragmented, low-height, non-convective fountain, to a glass-bearing lava flow activity reflect the sequential withdrawal of a zoned magma chamber with slight differences in pre-eruptive parameters (T and H_2O melt content) of the resident magma prior the eruption.

In addition, there is evidence for the existence of different pre-eruptive processes which affected the interior of this magma chamber as recorded by the zonation patterns of single feldspar crystals. The step zoning found in alkali feldspar crystals from the lavas (with An_{6-7} and An_4), indicates that this phase registered slight temperature variations of between 850 and 900 ºC (Fig. 6). As the zoning does not extend to other chemical elements, we can rule out the idea of contrasting compositional layers inside the main magmatic body.

Moreover, An-rich feldspar rims and microlites (Figs. 5-6) are indicators of higher temperatures (up to 950 ºC). This could have been caused by an external heat supply prior to eruption, possibly by a magma intrusion, which in turn could have triggered the event. This less evolved and hotter magma (1000-1050 ºC according to Ablay et al., 1998 and Martí et al. 2020) could have caused a temperature rise at the bottom of the resident magma, responsible

for the slight increase in the amount of FeO* (up to 1.4 wt.%) and CaO (up to An_{9-14}) observed in the alkali feldspar rims and microlites, and the increase of enstatite and Mg# in the rims of some clinopyroxenes. However, mingling/mixing between the two magma was rather restricted, as suggested by: 1) the presence of feldspar phenocrysts of evolved compositions (< 1.5 mol.% An) without calcium-rich rims in the explosive phase; 2) the low thickness (~ 5 μm) of the more mafic rims; and 3) the absence of banded pumices or the emission of hybrid magmas. Most likely, both magmas would only have coexisted for a short time (hours to few weeks) prior to the eruption. The consequent volatile exsolution from the more mafic magma disturbed the equilibrium in the magma chamber and produced a syn-eruptive "self-mixing" process (Couch et al., 2001; Triebold et al., 2006), which caused the extrusion of the main magma into the upper part of the chamber. This explains the presence of phenocrysts of very different compositions in the pumice samples and the rather similar bulk rock composition of both products.

According to the results obtained, the Pico Cabras eruption constitutes another documented example, together with those from Roques Blancos (Andújar et al., 2013), Montaña Blanca (Ablay et al., 1995; Andújar and Scaillet, 2012b), and El Palomar (Martí et al., 2020), of how rapidly Tenerife phonolitic magmas may enter into eruption when they receive an energy input from deeper magmas. Data presented here confirms that T-PV explosive flank dome eruptions are associated with very shallow magma batches and that they could be well anticipated with precise monitoring. Moreover, it is worth highlighting here the presence of sodalite in the explosive products from Pico Cabras, an indicator of the presence of a significant amount of halogen gases within the fluid phase. These gases (especially chlorine and, above all, bromine) play a large role in ozone layer depletion once they reach the stratosphere (Bureau et al., 2000; Cadoux et al., 2015, 2018; Daniel et al., 1999).

7. Conclusions.

In this work we have undertaken a study of the pre-eruptive conditions of the Pico Cabras dome eruption (Teide-Pico Viejo magmatic system, Tenerife) and their relation to the changes in eruptive dynamics during the eruption. The magma of this eruption was stored in a reservoir at 100 ± 50 MPa, which was chemically and thermally zoned. The main body would have had a temperature of 880 ± 30 ºC and 2.5-3 wt.% H_2O and it is the magma that gave rise to the lava flow phase at the end of the eruption. However, the initial eruptive phase that formed the pumice fall deposits and the dome structure derived from the upper part of the chamber, where magma was stored at 725-800 ºC and 3.5-5 wt.% H_2O. This data allows us to connect the evolution of the eruption with changes in temperature and the amount of volatiles within the reservoir.

The magmatic evolution of Teide-Pico Viejo volcanic system is likely to continue producing these kinds of explosive eruptions. Furthermore, the presence of feldspar relicts with a composition equivalent to those found in the Las Cañadas caldera episode in Pico Cabras most evolved products indicates that the current T-PV is already producing phonolites with a high explosive potential. An eruption with these characteristics would have a dramatic impact on Tenerife, particularly towards the north of the island. Therefore, there is a need to continue increasing our knowledge of the geological record and the processes occurring inside the active central volcanic system in order to be able to undertake an accurate hazard assessment of the island. In particular, studies regarding the volatile components of these magmas should be carried out in order to evaluate the effects they could have on atmospheric chemistry and, as a result, on human health.

Acknowledgements:

This study has been partially funded by EC Grant EVE (ref: DG ECHO H2020 826292), the Ministry of Science, Innovation, and Universities of Spain (FPU18/02572) and the CSIC grant JAEINT_18_00808. The authors kindly acknowledge the analytical SEM, EMPA and Microfluorescence support provided by I. Di Carlo and the financial support of Equipex-Planex ANR-11-EQPX-0036 and Labex-Voltaire ANR-10-LABX-100-01 from Orléans. Raffaello Cioni and an anonymous reviewer are kindly thanked for the extensive reviews of the original manuscript. We thank M. Roden for his help with the editorial handling of this work. Authors kindly thank S. Meletlidis, M.J. Blanco, and the IGN from the Canary Islands for their support provided during the field campaign. The help from M. Jiménez-Mejías, B. Scaillet, and M. Pichavant during sampling was highly appreciated. English text was corrected by Grant George Buffett of Terranova Scientific (www.terranova.barcelona).

Data Availability

Datasets related to this article can be found at http://dx.doi.org/10.20350/digitalCSIC/12715, hosted at the open-access repository DIGITAL.CSIC (Dorado *et al.*, 2020).

Declaration of interests

☒ The authors declare that they have no known competing financial interests or personal relationships that could have appeared to influence the work reported in this paper.

References.

Ablay, G.J., Martí, J., 2000. Stratigraphy, structure, and volcanic evolution of the Pico Teide-Pico Viejo formation, Tenerife, Canary Islands. Journal of Volcanology and Geothermal Research 103, 175–208. https://doi.org/10.1016/S0377-0273(00)00224-9

Ablay, G.J., Ernst, G.G.J., Marti, J., Sparks, R.S.J., 1995. The-2 ka subplinian eruption of Montaña Blanca, Tenerife. Bulletin of Volcanology 57, 337–355.

Ablay, G.J., Carroll, M.R., Palmer, M.R., Marti, J., Sparks, R.S.J., 1998. Basanite-Phonolite Lineages of the Teide-Pico Viejo Volcanic Complex, Tenerife, Canary Islands. Journal of Petrology 39, 905–936. https://doi.org/10.1093/petroj/39.5.905

Andújar, J., Scaillet, B., 2012a. Relationships between pre-eruptive conditions and eruptive styles of phonolite-trachyte magmas. Lithos 152, 122–131. https://doi.org/10.1016/j.lithos.2012.05.009

Andújar, J., Scaillet, B., 2012b. Experimental constraints on parameters controlling the difference in the eruptive dynamics of phonolitic magmas: The case of Tenerife (Canary islands). Journal of Petrology 53, 1777–1806. https://doi.org/10.1093/petrology/egs033

Andújar, J., Costa, F., Martí, J., Wolff, J.A., Carroll, M.R., 2008. Experimental constraints on the pre-eruptive conditions of the phonolitic magma from the caldera-forming the Abrigo eruption, Tenerife (Canary Islands). Chemical Geology 257, 173–191. https://doi.org/10.1016/j.chemgeo.2008.08.012

Andújar, J., Costa, F., Martí, J., 2010. Magma storage conditions of the last eruption of Teide volcano (Canary Islands, Spain). Bulletin of Volcanology 72, 381–395. https://doi.org/10.1007/s00445-009-0325-3

Andújar, J., Costa, F., Scaillet, B., 2013. Storage conditions and eruptive dynamics of central versus flank eruptions in volcanic islands: the case of Tenerife (Canary Islands, Spain). Journal of Volcanology and Geothermal Research 260, 62–79. https://doi.org/10.1016/j.jvolgeores.2013.05.004ï

Araña, V., Brändle, J.L., 1969. Variation trends in the alkaline salic rocks of Tenerife. Bulletin Volcanologique 33, 1145–1165. https://doi.org/10.1007/BF02597713

Beard, C.D., Van Hinsberg, V.J., Stix, J., Wilke, M., 2019. Clinopyroxene/Melt Trace Element Partitioning in Sodic Alkaline Magmas. Journal of Petrology 60, 1797–1823. https://doi.org/10.1093/petrology/egz052

Berndt, J., Holtz, F., Koepke, J., 2001. Experimental constraints on storage conditions in the chemically zoned phonolitic magma chamber of the Laacher See volcano. Contributions to Mineralogy and Petrology 140, 469–486. https://doi.org/10.1007/PL00007674

Boudon, G., Balcone-Boissard, H., Villemant, B., Morgan, D.J., 2015. What factors control superficial lava dome explosivity? Scientific Reports 5, 1–14. https://doi.org/10.1038/srep14551

Bryan, S.E., Martí, J., Leosson, M., 2002. Petrology and geochemistry of the Bandas des Sur Formation, Las Cañadas Edifice, Tenerife (Canary Islands). Journal of Petrology 43, 1815–1856. https://doi.org/10.1093/petrology/43.10.1815

Bureau, H., Keppler, H., Métrich, N., 2000. Volcanic degassing of bromine and iodine: Experimental fluid/melt partitioning data and applications to stratospheric chemistry. Earth and Planetary Science Letters 183, 51–60. https://doi.org/10.1016/S0012-821X(00)00258-2

Cadoux, A., Scaillet, B., Bekki, S., Oppenheimer, C., Druitt, T.H., 2015. Stratospheric Ozone destruction by the Bronze-Age Minoan eruption (Santorini Volcano, Greece). Scientific Reports 5. https://doi.org/10.1038/srep12243

Cadoux, A., Iacono-Marziano, G., Scaillet, B., Aiuppa, A., Mather, T.A., Pyle, D.M., Deloule, E., Gennaro, E., Paonita, A., 2018. The role of melt composition on aqueous fluid vs. silicate melt partitioning of bromine in magmas. Earth and Planetary Science Letters 498, 450–463. https://doi.org/10.1016/j.epsl.2018.06.038

Carracedo, J.C., Rodríguez Badiola, E., Guillou, H., Paterne, M., Scaillet, S., Pérez Torrado, F.J., Paris, R., Fra-Paleo, U., Hansen, A., 2007. Eruptive and structural history of Teide Volcano and rift zones of Tenerife, Canary Islands. Geological Society of America Bulletin 119, 1027–1051. https://doi.org/10.1130/B26087.1

Cashman, K. V., 2004. Volatile controls on magma ascent and eruption, in: The State of the Planet: Frontiers and Challenges in Geophysics. pp. 109–124. https://doi.org/10.1029/150GM10

Cassidy, M., Manga, M., Cashman, K., Bachmann, O., 2018. Controls on explosive-effusive volcanic eruption styles. Nature Communications. https://doi.org/10.1038/s41467-018-05293-3

Cooper, L.B., Bachmann, O., Huber, C., 2015. Volatile budget of Tenerife phonolites inferred from textural zonation of S-rich haüyne. Geology 43, 423–426. https://doi.org/10.1130/G36505.1

Couch, S., Sparks, R.S.J., Carroll, M.R., 2001. Mineral disequilibrium in lavas explained by convective self-mixing in open magma chambers. Nature 411, 1037–1039. https://doi.org/10.1038/35082540

Daniel, J.S., Solomon, S., Portmann, R.W., Garcia, R.R., 1999. Stratospheric ozone destruction: The importance of bromine relative to chlorine. Journal of Geophisical Research: Atmospheres 104, 871–894. https://doi.org/10.1029/1999JD900381

Deer, W.A., Howie, R.A., Zussman, J., 1972. Rock-forming Minerals, Volume 4. Framework silicates. Longman, Harlow.

Degruyter, W., Bachmann, O., Burgisser, A., Manga, M., 2012. The effects of outgassing on the transition between effusive and explosive silicic eruptions. Earth and Planetary Science Letters 349–350, 161–170. https://doi.org/10.1016/j.epsl.2012.06.056

Devine, J.D., Gardner, J.E., Brack, H.P., Layne, G.D., Rutherford, M.J., 1995. Comparison of microanalytical methods for estimating H20 contents of silicic volcanic glasses. American Mineralogist 80 (3–4), 319–328.

Dorado, O., Andújar, J., Martí, J., Geyer, A., 2020. Major elements geochemistry of Pico Cabras dome's explosive and effusive products (Tenerife) [Dataset]. DIGITAL.CSIC. https://doi.org/http://dx.doi.org/10.20350/digitalCSIC/12715

Eichelberger, J.C., Carrigan, C.R., Westrich, H.R., Price, R.H., 1986. Non-explosive silicic volcanism. Nature 323, 598–602. https://doi.org/10.1038/323598a0

Faranda, C.F., Di Carlo, I., Scaillet, B., Andújar, J., 2019. An X-Ray Micro-Fluorescence spectrometry analysis for determination of bromine content in alkaline rocks, in: Conference EMAS 2019 - 16th European Workshop on Modern Developments and Applications in Microbeam Analysis. At: Norwegian University of Technology and Science, Trondheim, Norway.

García, O., Bonadonna, C., Martí, J., Felpeto, A., Biolli, L., 2012. The 5,660 yBP Boquerón explosive eruption, Teide-Pico Viejo complex, Tenerife. Bulletin of Volcanology 74, 2037–2050. https://doi.org/10.1007/s00445-012-0646-5

García, O., Guzmán, S., Martí, J., 2014. Stratigraphic correlation of Holocene phonolitic explosive episodes of the Teide–Pico Viejo Volcanic Complex, Tenerife. Journal of the Geological Society 171, 375–387. https://doi.org/10.1144/jgs2013-086

Gonnermann, H.M., Manga, M., 2003. Explosive volcanism may not be an inevitable consequence of magma fragmentation. Nature 426, 432–435. https://doi.org/10.1038/nature02138

Lattard, D., 1995. Experimental evidence for the exsolution of ilmenite from titaniferous spinel. American Mineralogist 80, 968–981. https://doi.org/10.2138/am-1995-9-1013

Lavallée, Y., Dingwell, D.B., Johnson, J.B., Cimarelli, C., Hornby, A.J., Kendrick, J.E., Von Aulock, F.W., Kennedy, B.M., Andrews, B.J., Wadsworth, F.B., Rhodes, E., Chigna, G., 2015. Thermal vesiculation during volcanic eruptions. Nature 528, 544–547. https://doi.org/10.1038/nature16153

Le Bas, M.J., Le Maitre, R.W., Streckeisen, A., Zanettin, B., 1986. A Chemical Classification of Volcanic Rocks Based on the Total Alkali-Silica Diagram. Journal of petrology 27(3), 745–750.

Martel, C., Bourdier, J.L., Pichavant, M., Traineau, H., 2000. Textures, water content and degassing of silicic andesites from recent plinian and dome-forming eruptions at Mount Pelee volcano (Martinique, Lesser Antilles arc). Journal of Volcanology and Geothermal Research 96, 191–206. https://doi.org/10.1016/S0377-0273(99)00147-X

Martel, C., Brooker, R.A., Andújar, J., Pichavant, M., Scaillet, B., Blundy, J.D., 2017. Experimental simulations of magma storage and ascent, in: Gottsmann, J.N.J.S.B. (Ed.), Volcanic Unrest, from Science to Society. Springer, Cham., pp. 101–110.

Martí, J., 2019. Las Cañadas caldera, Tenerife, Canary Islands: A review, or the end of a long volcanological controversy. Earth-Science Reviews. https://doi.org/10.1016/j.earscirev.2019.102889

Martí, J., Gudmundsson, A., 2000. The Las Cañadas caldera (Tenerife, Canary Islands): an overlapping collapse caldera generated by magma-chamber migration. Journal of volcanology and geothermal research 103(1–4), 161–173. https://doi.org/https://doi.org/10.1016/S0377-0273(00)00221-3

Martí, J., Mitjavila, J., & Araña, V., 1994. Stratigraphy, structure and geochronology of the Las Cañadas caldera (Tenerife, Canary Islands). Geological Magazine, 131(6), 715-727. doi:10.1017/S0016756800012838

Martí, J., Geyer, A., Andújar, J., Teixidó, F., Costa, F., 2008. Assessing the potential for future explosive activity from Teide-Pico Viejo stratovolcanoes (Tenerife, Canary Islands). Journal of Volcanology and Geothermal Research 178, 529–542. https://doi.org/10.1016/j.jvolgeores.2008.07.011

Martí, J., Zafrilla, S., Andújar, J., Jiménez-Mejías, M., Scaillet, B., Pedrazzi, D., Doronzo, D., Scaillet, S., 2020. Controls of magma chamber zonation on eruption dynamics and deposits stratigraphy: The case of El Palomar fallout succession (Tenerife, Canary Islands). Journal of Volcanology and Geothermal Research 399, 106908. https://doi.org/10.1016/j.jvolgeores.2020.106908

Masotta, M., Mollo, S., Freda, C., Gaeta, M., Moore, G., 2013. Clinopyroxene-liquid thermometers and barometers specific to alkaline differentiated magmas. Contributions to Mineralogy and Petrology 166, 1545–1561. https://doi.org/10.1007/s00410-013-0927-9

Mollo, S., Masotta, M., Forni, F., Bachmann, O., De Astis, G., Moore, G., Scarlato, P., 2015. A K-feldspar-liquid hygrometer specific to alkaline differentiated magmas. Chemical Geology 392, 1–8. https://doi.org/10.1016/j.chemgeo.2014.11.010

Morimoto, N., 1988. Nomenclature of Pyroxenes. Mineralogy and Petrology 39, 55–76. https://doi.org/10.1007/BF01226262

Nakada, S., Motomura, Y., Shimizu, H., 1995. Manner of magma ascent at Unzen Volcano (Japan). Geophysical Research Letters 22, 567–570. https://doi.org/10.1029/95GL00002

Putirka, K.D., 2008. Thermometers and barometers for volcanic systems. Reviews in Mineralogy and Geochemistry 69, 61–120. https://doi.org/10.2138/rmg.2008.69.3

Putirka, K., 2016. Special collection: Rates and depths of magma ascent on earth: Amphibole thermometers and barometers for igneous systems and some implications for eruption

mechanisms of felsic magmas at arc volcanoes. American Mineralogist 101, 841–858. https://doi.org/10.2138/am-2016-5506

Schmidt, B.C., Behrens, H., 2008. Water solubility in phonolite melts: Influence of melt composition and temperature. Chemical Geology 256, 259–268. https://doi.org/10.1016/j.chemgeo.2008.06.043

Signorelli, S., Carroll, M.R., 2000. Solubility and fluid-melt partitioning of Cl in hydrous phonolitic melts. Geochimica et Cosmochimica Acta 64, 2851–2862. https://doi.org/10.1016/S0016-7037(00)00386-0

Sparks, R.S.J., 1978. The dynamics of bubble formation and growth in magmas: A review and analysis. Journal of Volcanology and Geothermal Research 3, 1–37. https://doi.org/10.1016/0377-0273(78)90002-1

Sparks, R.S.J., 1997. Causes and consequences of pressurisation in lava dome eruptions. Earth and Planetary Science Letters 150, 177–189. https://doi.org/10.1016/s0012-821x(97)00109-x

Triebold, S., Kronz, A., Wörner, G., 2006. Anorthite-calibrated backscattered electron profiles, trace elements and growth textures in feldspars from the Teide-Pico Viejo volcanic complex (Tenerife). Journal of Volcanology and Geothermal Research 154, 117–130. https://doi.org/10.1016/j.jvolgeores.2005.09.023

Wellman, T.R., 1970. The stability of sodalite in a synthetic syenite plus aqueous chloride fluid system. Journal of Petrology 11, 49–72. https://doi.org/10.1093/petrology/11.1.49

Wilson, L., Sparks, R.S.J., Walker, G.P.L., 1980. Explosive volcanic eruptions -- IV. The control of magma properties and conduit geometry on eruption column behaviour. Geophysical Journal International 63, 117–148. https://doi.org/10.1111/j.1365-246X.1980.tb02613.x

Wolff, J.A., 1985. Zonation, mixing and eruption of silica-undersaturated alkaline magma: A case study from Tenerife, Canary Islands. Geological Magazine 122, 623–640. https://doi.org/10.1017/S0016756800032039

Wolff, J.A., 1987. Crystallisation of nepheline syenite in a subvolcanic magma system: Tenerife, canary islands. LITHOS 20, 207–223. https://doi.org/10.1016/0024-4937(87)90009-0

Wolff, J.A., Storey, M., 1984. Zoning in highly alkaline magma bodies. Geological Magazine 121, 563–575. https://doi.org/10.1017/S0016756800030715

Wolff, J.A., Toney, J.B., 1993. Trapped liquid from a nepheline syenite: a re-evaluation of Na-, Zr-, F-rich interstitial glass in a xenolith from Tenerife, Canary Islands. LITHOS 29, 285–293. https://doi.org/10.1016/0024-4937(93)90022-5

Woods, A.W., Koyaguchi, T., 1994. Transitions between explosive and effusive eruptions of silicic magmas. Nature 370, 641–644. https://doi.org/10.1038/370641a0

Web references:

DIGITAL.CSIC repository. http://digital.csic.es/

IGN seismic catalogue: http://www.ign.es/web/ign/portal/sis-catalogo-terremotos

System for Earth Sample Registration database: http://www.geosamples.org/

Fig. 1. Simplified geological and volcanostratigraphy of Tenerife. DRZ: Dorsal Rift Zone; PC: Pico Cabras; PV: Pico Viejo; SRZ: Santiago del Teide Rift Zone; SVZ: South Volcanic Zone; T: Teide. Modified from Martí et al. (2008).

Fig. 2. A and B) View of Pico Cabras dome, located on the north flank of Teide volcano. C) View of the different Pico Cabras deposits (dome, lava flow, and pumices) below

the Lavas Negras lava flow (last Teide eruption). Red dashed line marks the contact between Pico Cabras products and the Lavas Negras lava flow.

Fig. 3. Back-scattered electron images of representative mineral phases from Pico Cabras (A-F: lava flow samples, and G-I: pumice samples). A) Feldspar (Fsp) phenocryst with biotite (Bt) inclusions; B) Clinopyroxene (Cpx) phenocryst associated with smaller ilmenite (Ilm) with apatite (Ap) inclusions; C) Magnetite (Mt) phenocrysts with ilmenite exsolutions and apatite inclusions; D) Feldspar phenocryst associated with a smaller clinopyroxene; E) Rounded biotite associated with small oxides (magnetite and ilmenite); F) Amphibole (Amp) xenocryst associated with biotites and magnetite with ilmenite exsolutions; G) Biotite phenocryst with apatite inclusions; H) Sodalite (Sdl) phenocryst with sulphides, fluid, and glass inclusions; I) Feldspar phenocryst with small oxides and apatite inclusions.

Fig. 4. Feldspar compositions of all analysed feldspars from Pico Cabras eruption (Deer et al., 1972). The blue arrow shows the compositional evolution in a phonolitic magma of feldspars.

Fig. 5. Histograms of feldspar compositions expressed as anorthite (An), albite (Ab), and orthoclase (Or) content. A-C: composition of phenocryst cores. D-F: composition of microlites and phenocryst rims.

Fig. 6. Zoning profiles showing compositional variations within feldspar phenocrysts from both effusive (A, B) and explosive (C) phases. Top: back-scattered electron images of the phenocrysts showing the profile position. Blue vertical bands mark the boundaries between zones of different chemical compositions.

Fig. 7. FeO* (wt.%) vs. log (Or/An) for Pico Cabras feldspars. The blue arrow indicates the fractionation trend. Modified from Triebold et al. (2006).

Fig. 8. A) Classification diagram of clinopyroxenes (Morimoto, 1988) from Pico Cabras samples. En, Wo, and Fs refer to enstatite, wollastonite, and ferrosilite respectively. B) Zoning profiles of one of the few clinopyroxenes showing core-to-rim variation.

Fig. 9. Harker diagrams (SiO_2-K_2O-TiO_2-Al_2O_3 vs. Mg#) of Pico Cabras biotites. The black arrow marks the core-rim variation.

Fig. 10. Total alkali-silica classification diagram (Le Bas et al., 1986) for whole-rock and residual melt analyses from both the explosive and effusive phases. The black arrow indicates the evolutionary trend of the phonolitic magma. All analyses have been recalculated to 100%.

Fig. 11. Results of pre-eruptive parameter calculations using Martí et al. (2020), Mollo et al. (2015) and Masotta et al. (2013) empirical equations (see text). Panels on the right display kernel density estimates of calculated crystallization temperatures (a, c), water content (b), and pressure (d). Dashed lines represent mean values for P-T-H_2O estimates. Error bars for each parameter are also shown.

Fig. 12. Anorthite (mol.%) vs. water content diagram for Pico Cabras feldspar phenocrysts. Water content was obtained using the geohygrometer of Mollo et al. (2015), based on alkali feldspar and melt compositions.

Fig. 13. P-T data obtained using the geothermobarometer of Masotta et al. (2013), based on clinopyroxene composition and clinopyroxene liquid equilibria. Blue and orange crosses indicate the calculated model errors from the lava and pumices.

Fig. 14. S-N schematic cross section of the Teide-Pico Viejo complex and the Pico Cabras dome (the horizontal scale is equal to vertical scale). The scheme shows the location of the reservoirs for central Teide magmas (Andújar et al., 2010) and Pico Cabras magmas.

Pre-eruptive conditions estimated here in the different levels of the magma chamber are also shown. Magma reservoir volumes are not to scale.

Appendix A. Measured and predicted Or-Ab partition coefficient in K-feldspar-liquid pairs from Pico Cabras products used as an equilibrium test by Mollo et al. (2015) geohygrometer. The model assumes as reliable the compositions plotting within 10% of the 1:1 line (± 0.1).

Table 1. Major element composition and end-members of representative feldspars from Pico Cabras effusive (lava) and explosive (pumices) phases. Calculated H_2O using the Mollo et al. (2015) geohygrometer are also shown.

Sample	Lava	Lava	Lava	Lava	Lava	Lava	Lava	Pumice	Pumice	Pumice	Pumice	Pumice	Pumice
IGSN	IEODG0001	IEODG0001	IEODG0002	IEODG0001	IEODG0002	IEODG0001	IEODG0002	IEODG0003	IEODG0003	IEODG0003	IEODG0003	IEODG0003	IEODG0003
Zone	Core	Core	Core	Rim	Rim	Microlite	Microlite	Core	Core	Core	Rim	Microlite	Microlite
Analysis	PC1-01-34	PC1-02-115	PC2-05-59	PC1-01-51	PC2-10-124	PC1-01-72	PC2-04-21	PB-03-109	PB-02-86	PB-01-63	PB-02-92	PA-15-19	PC-05-7
SiO_2	64.18	65.35	64.94	63.84	67.16	63.20	65.32	66.37	67.01	66.89	66.45	65.64	64.42
TiO_2	0.03	0.09	0.03	0.49	0.26	0.37	0.16	0.13	0.00	0.01	0.07	0.51	0.54
Al_2O_3	20.59	19.52	20.07	20.85	18.77	20.19	19.18	19.65	18.82	19.16	18.76	19.94	20.55
MgO	0.02	0.00	0.03	0.01	0.00	0.02	0.01	0.02	0.00	0.04	0.00	0.05	0.04
CaO	1.49	0.90	1.39	2.13	0.46	2.39	0.69	0.99	0.18	0.10	0.20	0.84	2.76
FeO	0.39	0.22	0.34	0.53	0.26	0.80	0.43	0.34	0.32	0.14	0.13	0.65	1.35
Na_2O	8.10	7.96	7.97	7.79	7.42	7.91	7.28	7.78	6.63	7.43	6.90	6.11	8.50

K_2O	4.24	5.01	3.96	3.78	5.99	3.26	6.41	4.84	6.60	6.29	6.41	5.97	2.14
Sum	99.04	99.09	98.90	99.42	100.36	98.21	99.64	100.24	99.66	100.05	98.96	99.72	100.38
An	7.05	4.24	6.77	10.29	2.18	11.62	3.20	4.77	0.89	0.47	0.99	4.43	13.34
Ab	69.14	67.71	70.28	68.02	63.91	69.52	61.30	67.58	59.87	63.95	61.46	58.14	74.36
Or	23.81	28.05	22.95	21.69	33.91	18.87	35.50	27.64	39.24	35.58	37.55	37.43	12.30
H_2O*	3.06	3.95	3.09	2.51	4.67	1.99	4.27	4.28	5.47	6.16	6.24	4.58	1.37

*H_2O were obtain using the geogygrometer of Mollo *et al., (2015)*

Table 2. Major element composition, end-members, and Mg# of representative clinopyroxenes from the Pico Cabras lavas and pumices.

Sample	Lava	Lava	Lava	Lava	Lava	Pumices	Pumices	Pumices	Pumices	Pumices
IGSN	IEODG0001	IEODG0001	IEODG0001	IEODG0001	IEODG0001	IEODG0003	IEODG0003	IEODG0003	IEODG0003	IEODG0003
Zone	Core	Core	Core	Rim	Rim	Core	Core	Core	Rim	Rim
Analysis	PC1-10-126	PC1-10-139	PC1-06-63	PC1-06-76	PC1-10-123	PC-07-17	PC-13-31	PC-13-34	PC-13-28	PC-13-36
SiO_2	49.93	52.87	53.12	51.39	51.46	52.03	50.31	51.59	51.97	51.42
TiO_2	1.54	0.72	0.84	0.83	0.83	0.65	0.67	0.51	0.77	0.51
Al_2O_3	2.24	1.21	1.48	1.64	1.64	0.95	0.85	1.18	1.08	1.11
MgO	12.75	13.64	13.28	12.98	13.28	12.90	9.05	10.49	9.95	11.00
CaO	21.19	22.14	21.95	22.06	22.24	21.73	19.80	20.47	20.03	20.81
MnO	0.85	0.58	0.69	0.62	0.71	1.06	1.39	1.00	1.07	1.01
FeO	9.14	7.98	8.09	7.89	8.56	9.23	14.21	11.91	12.10	11.52
Na_2O	1.23	0.97	1.08	1.15	1.06	1.10	2.56	2.02	2.41	1.67
K_2O	0.05	0.00	0.00	0.00	0.05	0.02	0.023	0.02	0.00	0.01
Sum	98.91	100.10	100.62	98.54	99.83	99.66	98.85	99.17	99.39	99.05
En	38.51	40.07	39.53	39.02	38.97	38.28	28.95	32.89	31.96	33.93
Fs	15.48	13.15	13.50	13.31	14.10	15.37	25.51	20.96	21.80	19.93

Wo	46.01	46.77	46.97	47.67	46.93	46.36	45.54	46.15	46.24	46.14
#Mg	71.32	75.29	74.54	74.56	73.44	71.35	53.17	61.08	59.44	62.99

Table 3. Major element composition of representative biotites, magnetites, ilmenites, and sodalites from the Pico Cabras lavas and pumices. Mg# for biotites is also shown.

Mineral	Biotite					Magnetite*		Ilmenite		Sodalite	
Sample	Lava	Lava	Pumices	Pumices	Pumices	Lava	Pumices	Lava	Pumices	Pumices	Pumices
IGSN	IEODG0001	IEODG0001	IEODG0003	IEODG0003	IEODG0003	IEODG0001	IEODG0003	IEODG0001	IEODG0003	IEODG0003	IEODG0003
Zone	Core	Core	Core	Core	Rim	Core with exsolutions		Core	Core	Core	Rim
Analysis	PC1-11-185	PC2-01-53	PA-02-07	PA-28-33	PA-49-46	PC1-02-91	PC-13-25	PC1-06-53	PC-04-12	PC-PS-98	PC-PS-130
SiO_2	37.33	37.04	36.79	36.96	38.52	0.00	0.08	0.04	0.00	37.29	37.34
TiO_2	7.52	7.55	7.62	7.46	7.52	9.75	14.14	48.81	50.77	s.d	s.d
Al_2O_3	13.05	12.25	12.90	13.76	13.58	1.53	0.70	0.11	0.06	29.76	29.97
MgO	14.31	14.14	13.83	13.97	11.29	1.68	0.94	3.67	2.80	s.d	s.d
MnO	0.34	0.43	0.23	0.39	0.63	2.30	2.79	3.06	3.39	s.d	s.d
FeO	13.40	12.64	14.72	14.23	15.64	83.69	77.43	44.10	43.57	0.81	0.15
CaO	0.00	0.00	0.00	0.00	0.11	0.00	0.02	0.03	0.03	0.26	0.29
Na_2O	0.93	1.03	1.11	1.09	0.81	0.03	0.05	0.04	0.04	22.76	23.11
K_2O	8.66	8.61	8.37	8.49	8.23	0.06	0.03	0.00	0.00	1.91	1.84
Cl	n.d	n.d	0.04	0.05	0.07	n.d	0.00	n.d	n.d	6.67	6.86
SO_3	n.d	n.d	n.d	n.d	n.d	n.d	n.d	n.d	n.d	0.59	0.33
Sum	95.58	93.67	95.60	95.49	97.32	98.98	96.10	99.83	100.60	100.04	99.89
#Mg	65.56	66.61	62.61	63.65	56.27						
Mt						72.78	59.24	18.28	12.21		

wt.
%
n.d: no data. *Magnetite analysis do not represent pure magnetite composition, as they are contaminated by ilmenite exsolutions (see text).

Table 4. Major element composition of representative whole rock and residual melt analyses from the Pico Cabras lavas and pumices. Water content calculated using the method by difference (Devine et al., 1995) and temperatures calculated by Martí et al. (2020) geothermometer are also shown.

Sample	W.R. Lava	W.R. Pumice	R.M. Lava	R.M. Lava	R.M. Lava	R.M. Pumice	R.M. Pumice	R.M. Pumice	Inclusion
IGSN	IEOD G0001	IEOD G0003	IEOD G0001	IEOD G0001	IEOD G0001	IEOD G0003	IEOD G0003	IEOD G0003	IEOD G0001
Analysis	PC1-SM-22	P-SM-12	PC1-10-283	PC1-10-302	PC1-01-69	PA-04-27	PB-07-20	PB-07-13	PC1-06-01
SiO_2	60.78	61.22	57.81	56.01	55.50	59.72	59.93	59.43	56.82
TiO_2	0.91	0.64	0.92	1.11	1.07	0.69	0.64	0.63	0.86
Al_2O_3	19.02	19.34	19.11	18.46	18.37	18.98	18.78	19.05	18.26
MgO	0.46	0.45	0.59	0.79	0.97	0.38	0.35	0.34	2.18
CaO	0.97	0.80	0.39	0.35	0.29	0.55	0.70	0.64	0.24
MnO	0.14	0.12	0.39	0.32	0.65	0.32	0.17	0.31	0.26
FeO	3.71	3.27	4.74	4.97	5.20	3.61	3.53	3.33	8.42
Na_2O	8.58	8.61	10.53	11.71	11.59	9.66	9.60	9.66	5.67
K_2O	5.39	5.11	5.09	6.21	6.27	5.62	5.89	5.94	7.06
Cl	n.d	0.13	n.d	n.d	n.d	0.39	0.24	0.29	n.d
Sum	100.00	100.00	100.00	100.00	100.00	100.00	100.00	100.00	100.00
Original sum	99.23	99.06	99.88	98.77	97.80	99.02	98.97	97.14	99.61
Na_2O+K_2O	13.97	13.72	15.93	17.92	17.86	15.28	15.49	15.60	12.72
H_2O wt.%	0.77	0.92	0.12	1.23	2.20	0.98	1.03	2.86	0.39
T (ºC)	919	856	812	839	816	823	834	832	665

n.d. = no data. W.R. = Whole rock. R.M. = Residual melt. Water content calculated using the method by difference (Devine *et al.*, 1995). Temperatures from Martí et al., (2020)

Highlights:

- Pre-eruptive parameters play an important role in eruption dynamics.
- Accurate modelisation of P-T-H2O conditions requires phase equilibria experiments.
- Temperature and H_2O content controlled Pico Cabras explosive-effusive activity.

- Pico Cabras stratified chamber was trigger by an intermediate intrusion.
- T-PV system is already producing phonolites with a high explosive potential.

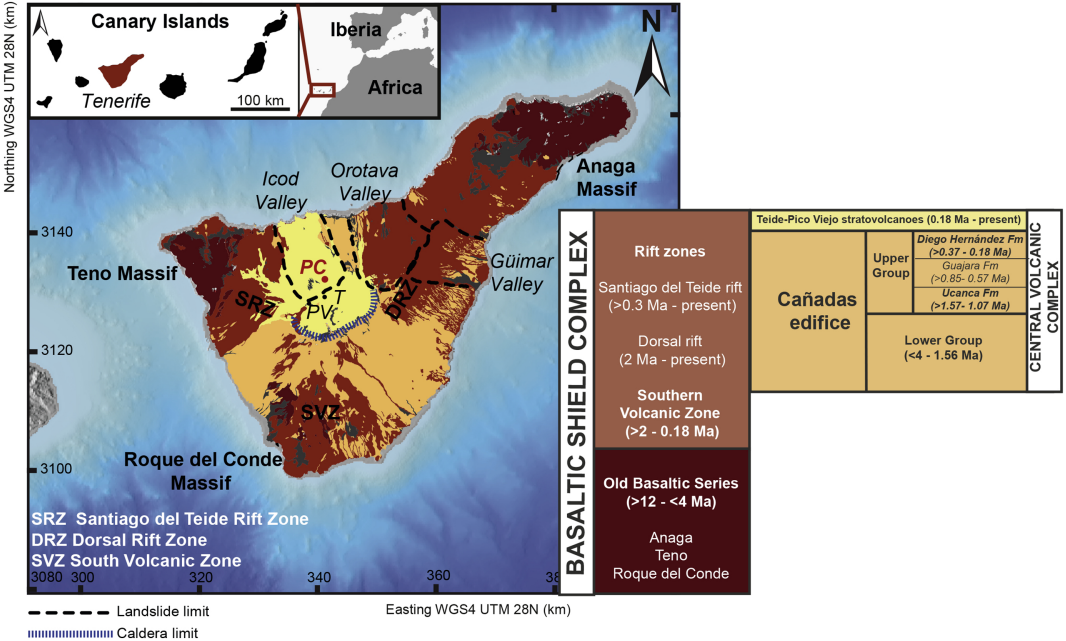
Canary Islands
Tenerife
100 km
Iberia
Africa
N
Icod Valley
Orotava Valley
Anaga Massif
Güimar Valley
Teno Massif
PC
PVt
SRZ
DRZ
SVZ
Roque del Conde Massif
3140
3120
3100
3080
300
320
340
360
SRZ Santiago del Teide Rift Zone
DRZ Dorsal Rift Zone
SVZ South Volcanic Zone
Northing WGS4 UTM 28N (km)
Easting WGS4 UTM 28N (km)
Landslide limit
Caldera limit
BASALTIC SHIELD COMPLEX
Rift zones
Santiago del Teide rift (>0.3 Ma - present)
Dorsal rift (2 Ma - present)
Southern Volcanic Zone (>2 - 0.18 Ma)
Old Basaltic Series (>12 - <4 Ma)
Anaga
Teno
Roque del Conde
Teide-Pico Viejo stratovolcanoes (0.18 Ma - present)
Cañadas edifice
Upper Group
Diego Hernández Fm (>0.37 - 0.18 Ma)
Guajara Fm (>0.85- 0.57 Ma)
Ucanca Fm (>1.57- 1.07 Ma)
Lower Group (<4 - 1.56 Ma)
CENTRAL VOLCANIC COMPLEX

Figure 1

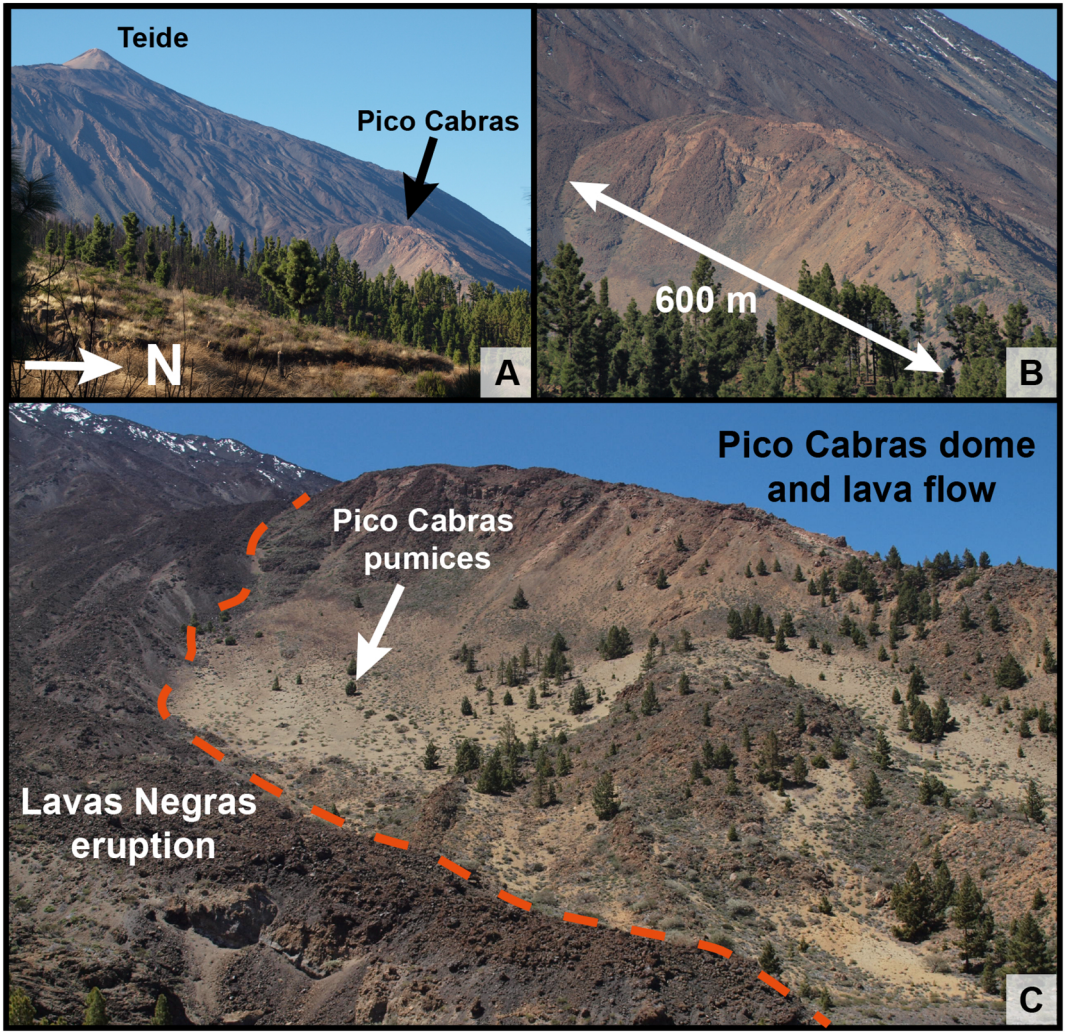
Teide
Pico Cabras
N
A
600 m
B
Pico Cabras dome
and lava flow
Pico Cabras
pumices
Lavas Negras
eruption
C

Figure 2

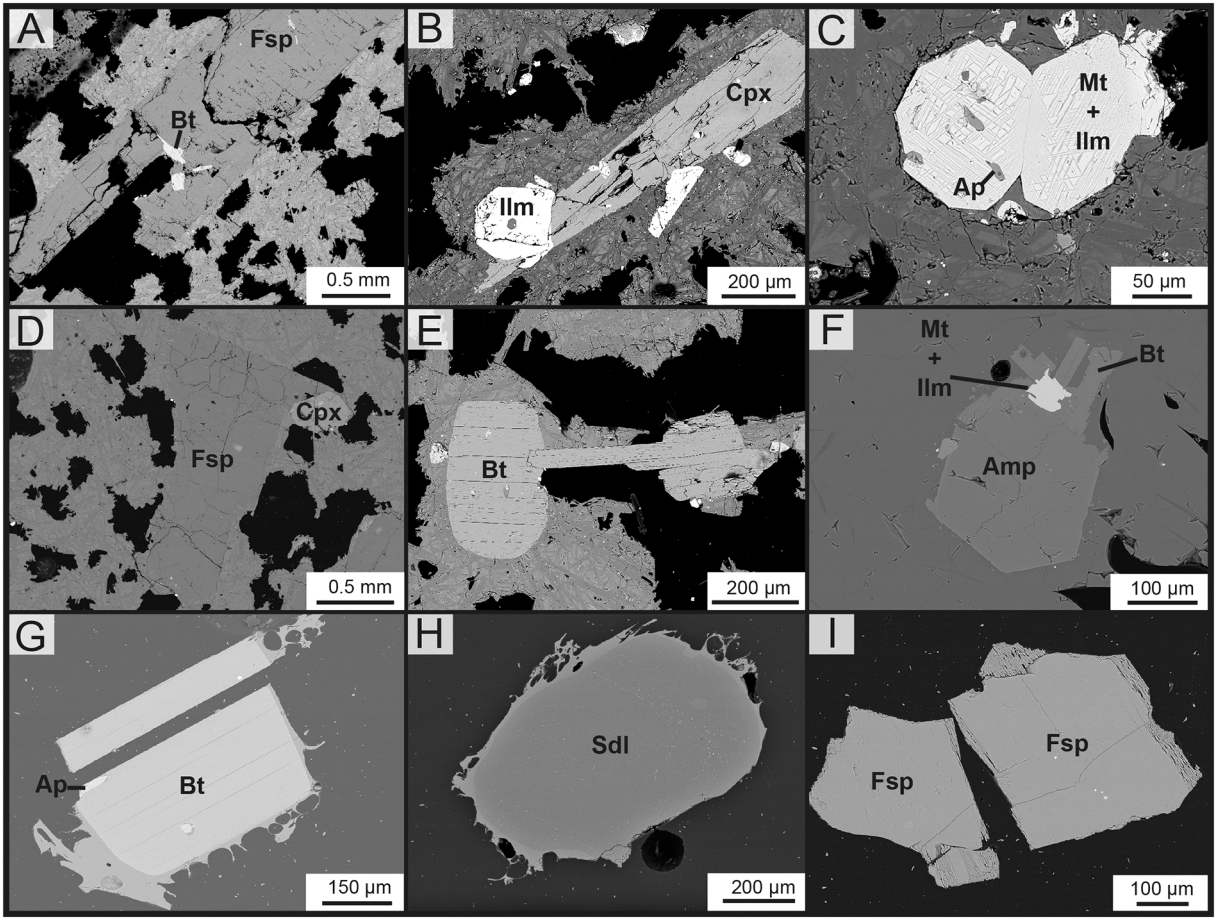
A
Fsp
Bt
0.5 mm
B
Cpx
Ilm
200 µm
C
Mt
+
Ilm
Ap
50 µm
D
Cpx
Fsp
0.5 mm
E
Bt
200 µm
F
Mt
+
Ilm
Bt
Amp
100 µm
G
Ap
Bt
150 µm
H
Sdl
200 µm
I
Fsp
Fsp
100 µm

Figure 3

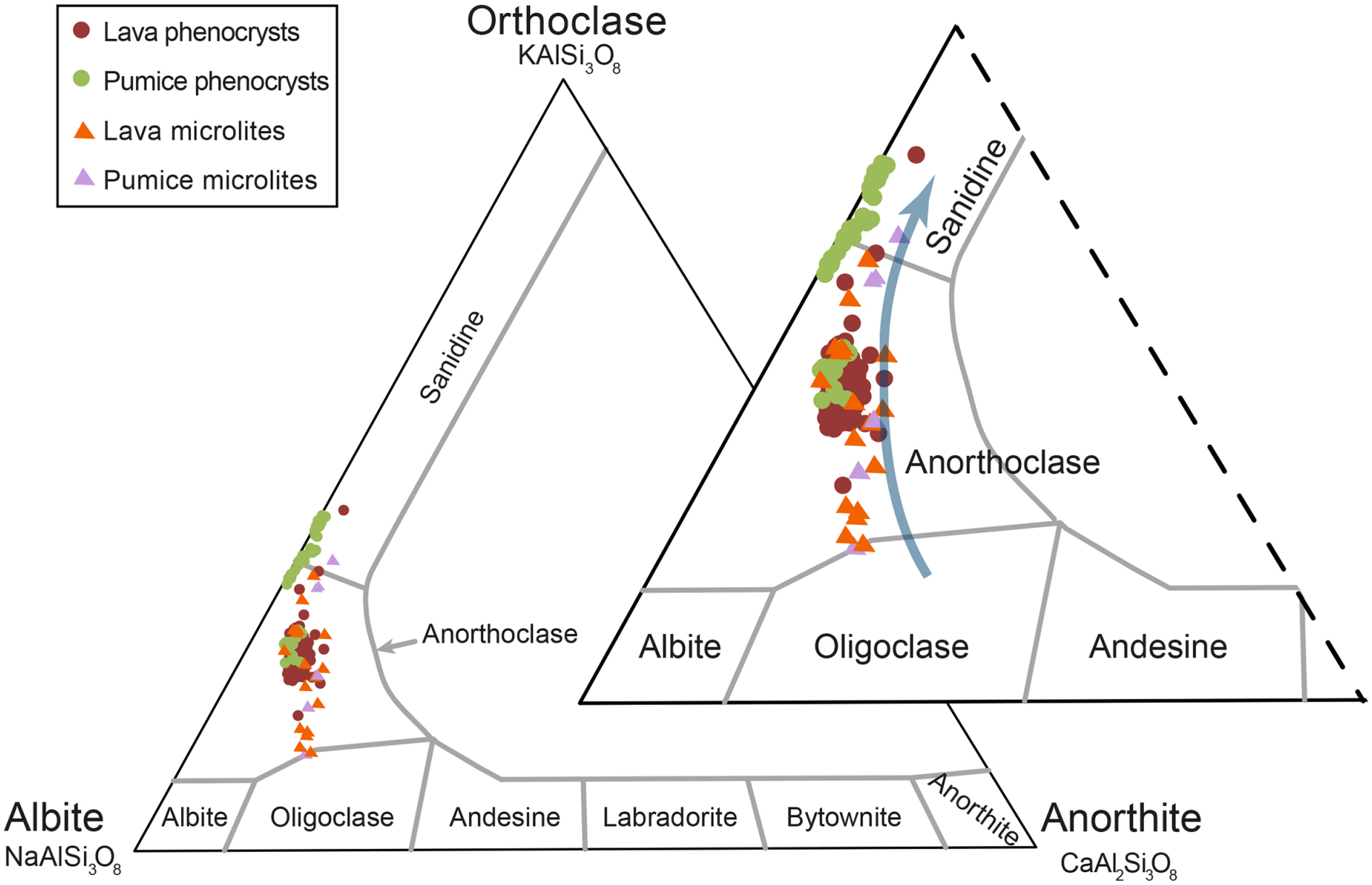
Lava phenocrysts
Pumice phenocrysts
Lava microlites
Pumice microlites
Orthoclase
KAlSi3O8
Sanidine
Anorthoclase
Albite
Oligoclase
Andesine
Labradorite
Bytownite
Anorthite
Albite
NaAlSi3O8
Anorthite
CaAl2Si3O8

Figure 4

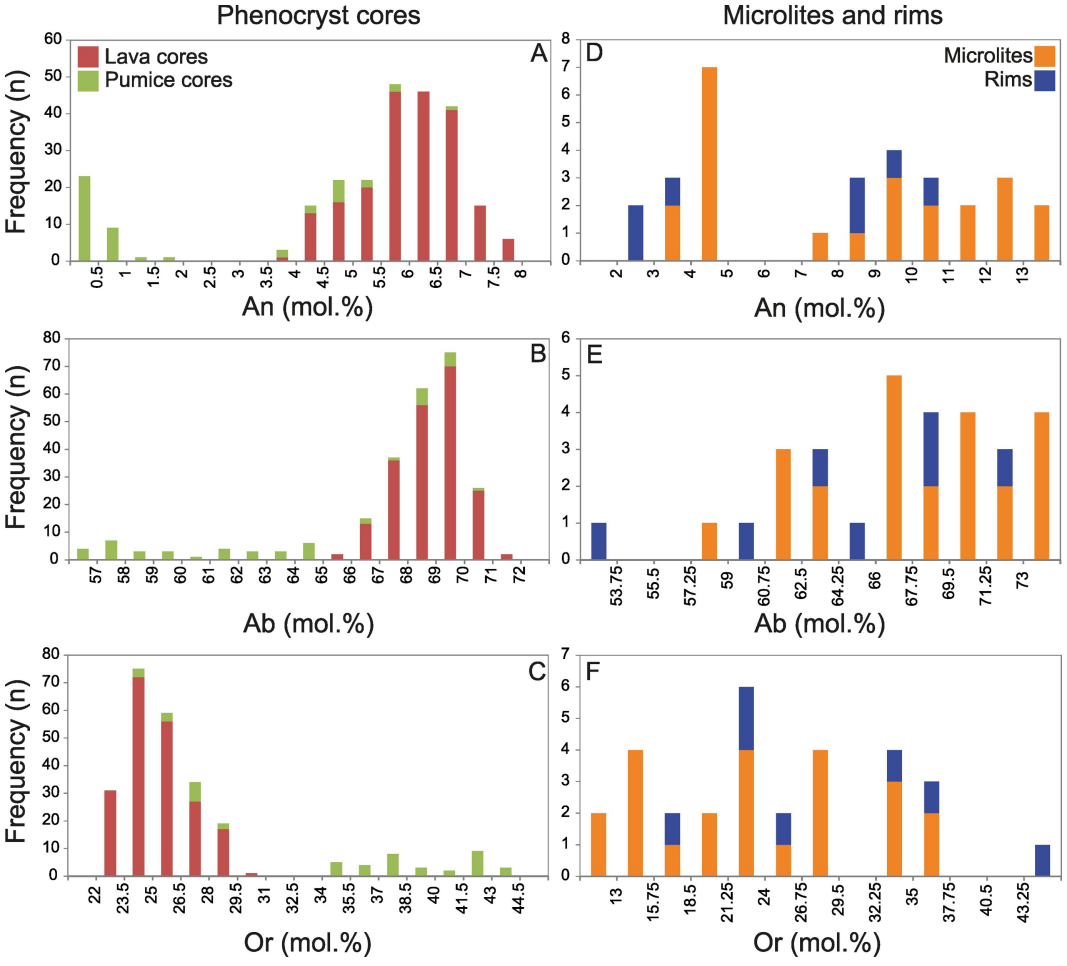
Phenocryst cores
Microlites and rims
Lava cores
Pumice cores
Microlites
Rims
A
B
C
D
E
F
Frequency (n)
An (mol.%)
Ab (mol.%)
Or (mol.%)

Figure 5

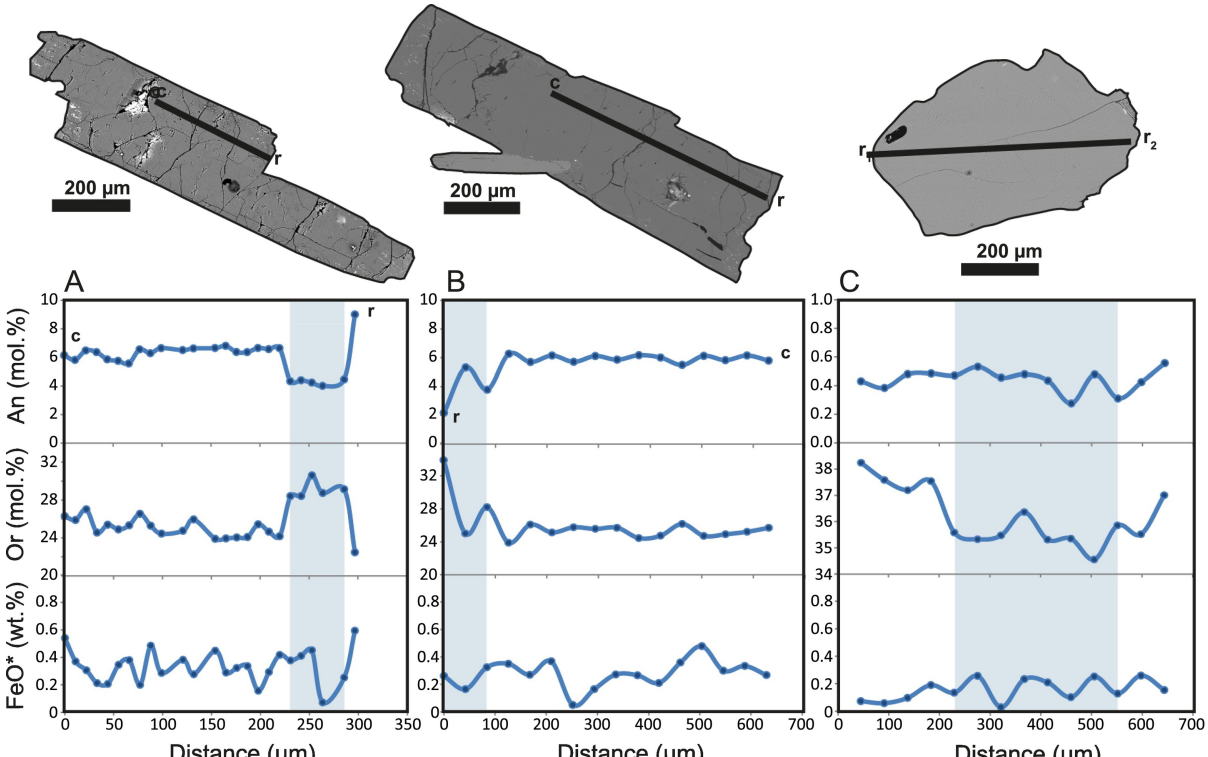
c
r
200 µm
c
r
200 µm
r1
r2
200 µm
A
B
C
An (mol.%)
Or (mol.%)
FeO* (wt.%)
Distance (µm)
Distance (µm)
Distance (µm)

Figure 6

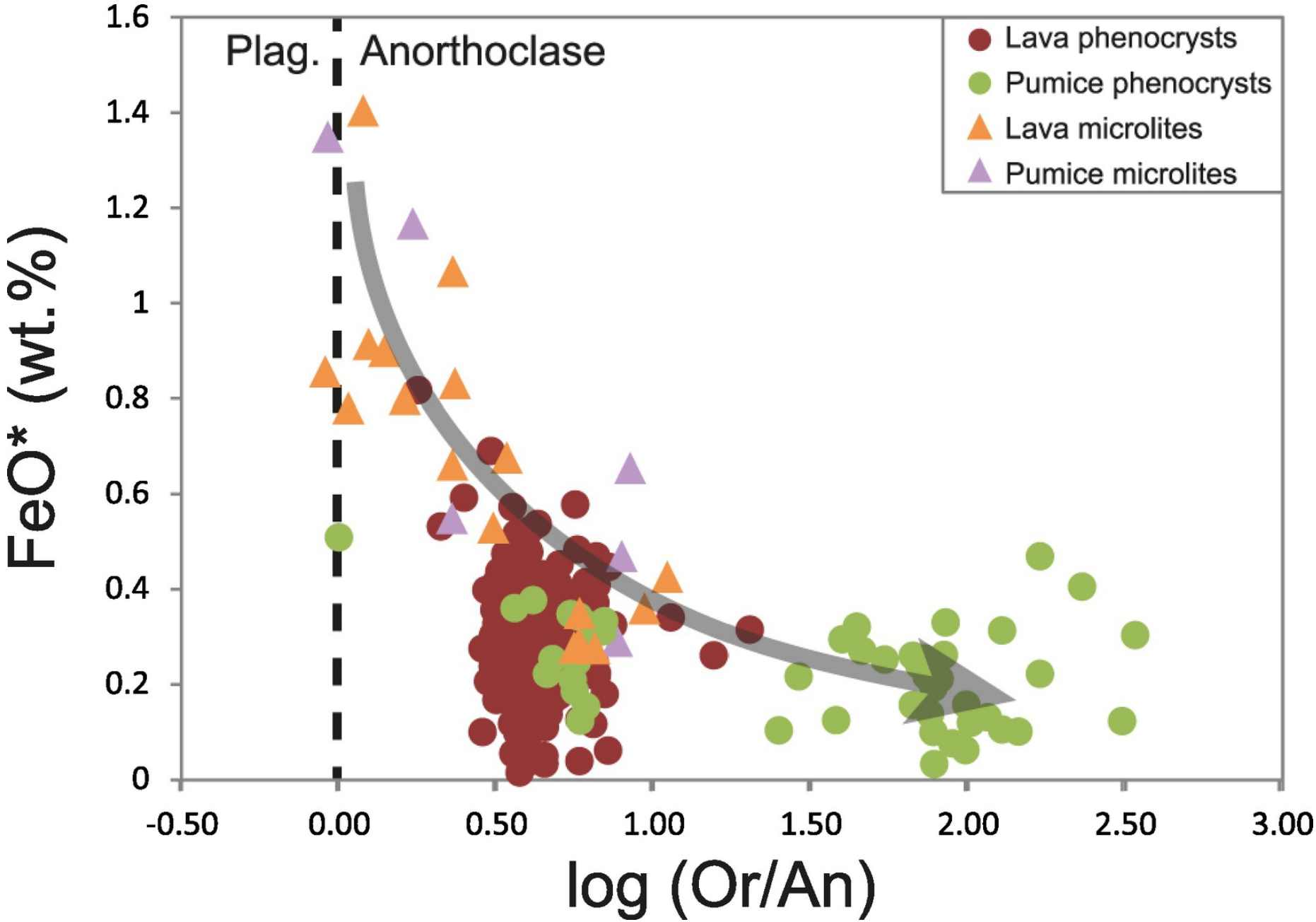
Plag.
Anorthoclase
Lava phenocrysts
Pumice phenocrysts
Lava microlites
Pumice microlites
FeO* (wt.%)
log (Or/An)
1.6
1.4
1.2
1
0.8
0.6
0.4
0.2
0
-0.50
0.00
0.50
1.00
1.50
2.00
2.50
3.00

Figure 7

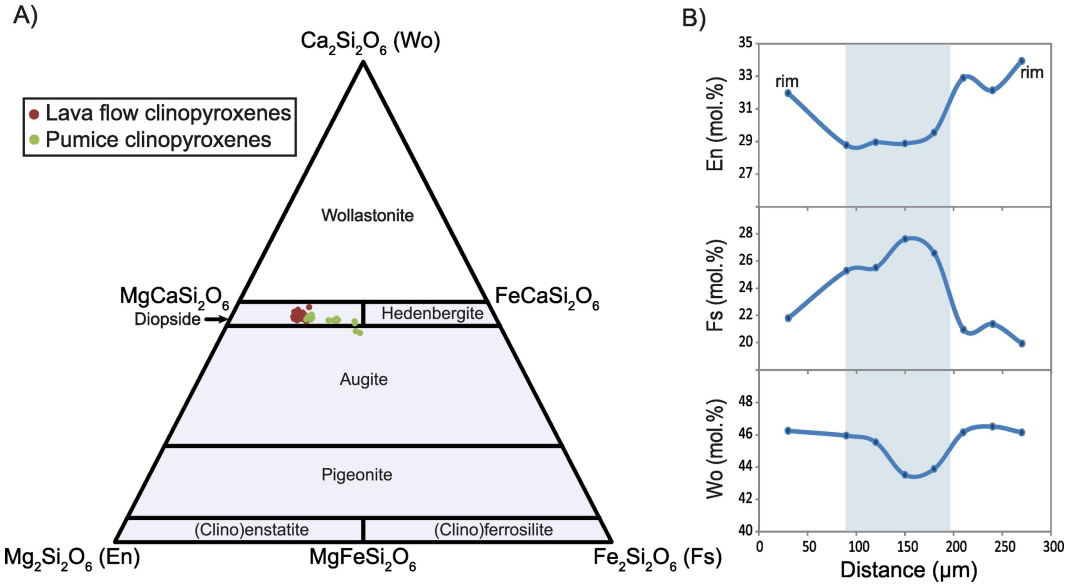
A)
$Ca_2Si_2O_6$ (Wo)
Lava flow clinopyroxenes
Pumice clinopyroxenes
Wollastonite
$MgCaSi_2O_6$
Diopside
$FeCaSi_2O_6$
Hedenbergite
Augite
Pigeonite
(Clino)enstatite
(Clino)ferrosilite
$Mg_2Si_2O_6$ (En)
$MgFeSi_2O_6$
$Fe_2Si_2O_6$ (Fs)
B)
rim
rim
En (mol.%)
Fs (mol.%)
Wo (mol.%)
Distance (μm)

Figure 8

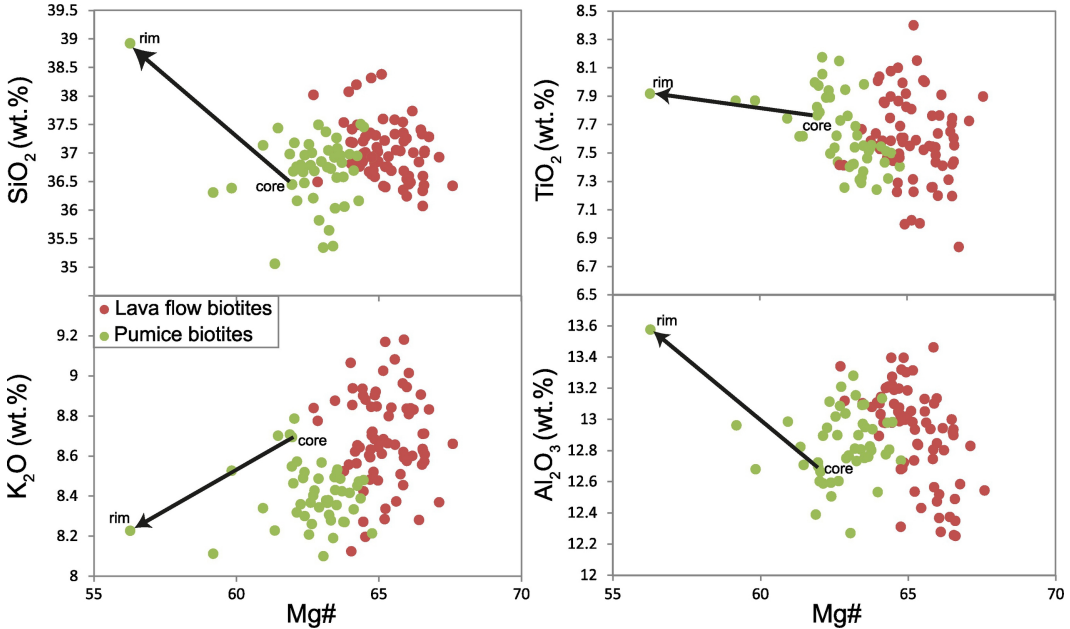
SiO2 (wt.%)
TiO2 (wt.%)
K2O (wt.%)
Al2O3 (wt.%)
Mg#
Mg#
rim
core
Lava flow biotites
Pumice biotites

Figure 9

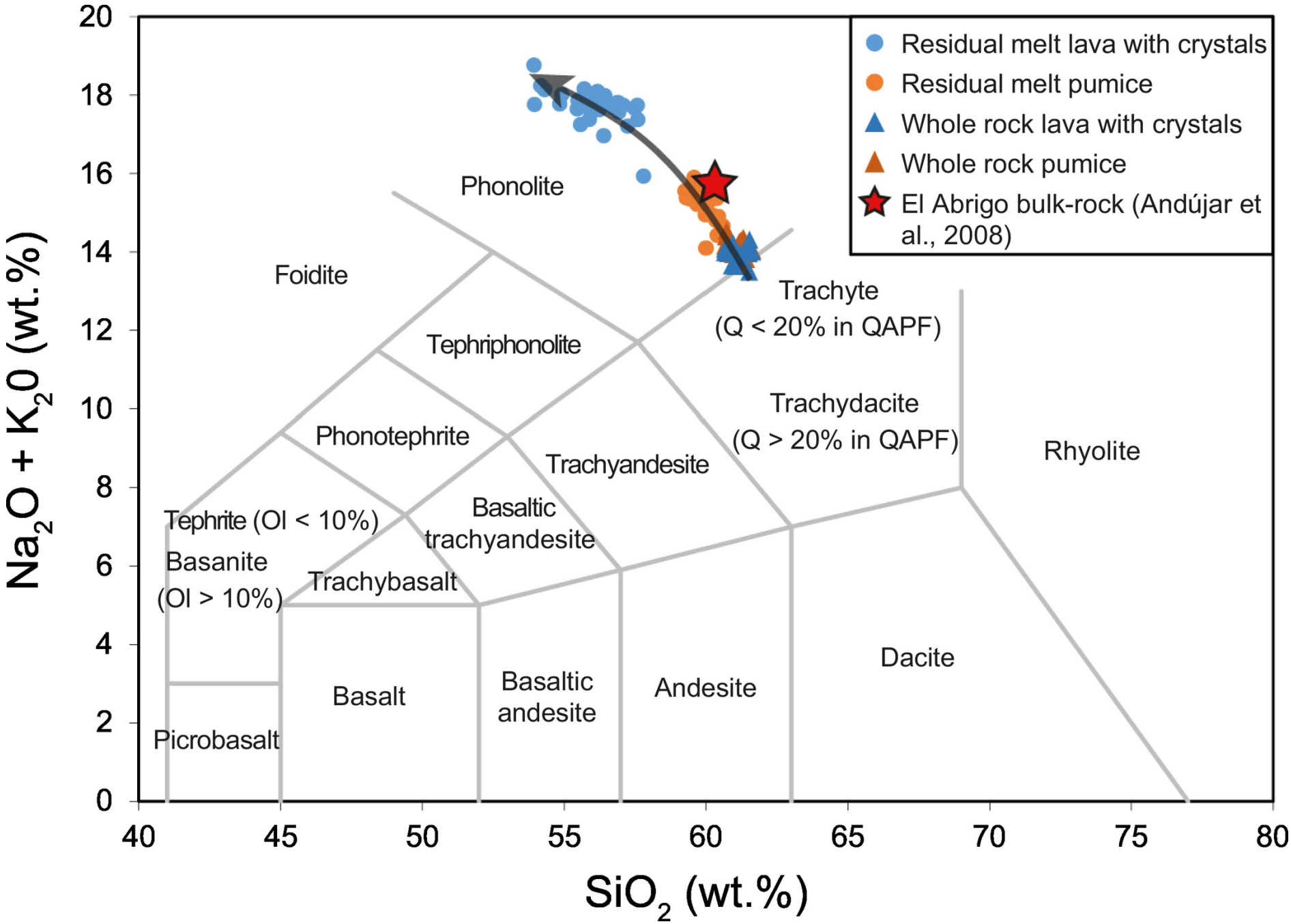
Residual melt lava with crystals
Residual melt pumice
Whole rock lava with crystals
Whole rock pumice
El Abrigo bulk-rock (Andújar et al., 2008)
Phonolite
Foidite
Tephriphonolite
Trachyte
(Q < 20% in QAPF)
Trachydacite
(Q > 20% in QAPF)
Rhyolite
Phonotephrite
Trachyandesite
Basaltic
trachyandesite
Tephrite (Ol < 10%)
Basanite
(Ol > 10%)
Trachybasalt
Dacite
Basalt
Basaltic
andesite
Andesite
Picrobasalt
$Na_2O + K_2O$ (wt.%)
SiO_2 (wt.%)
0
2
4
6
8
10
12
14
16
18
20
40
45
50
55
60
65
70
75
80

Figure 10

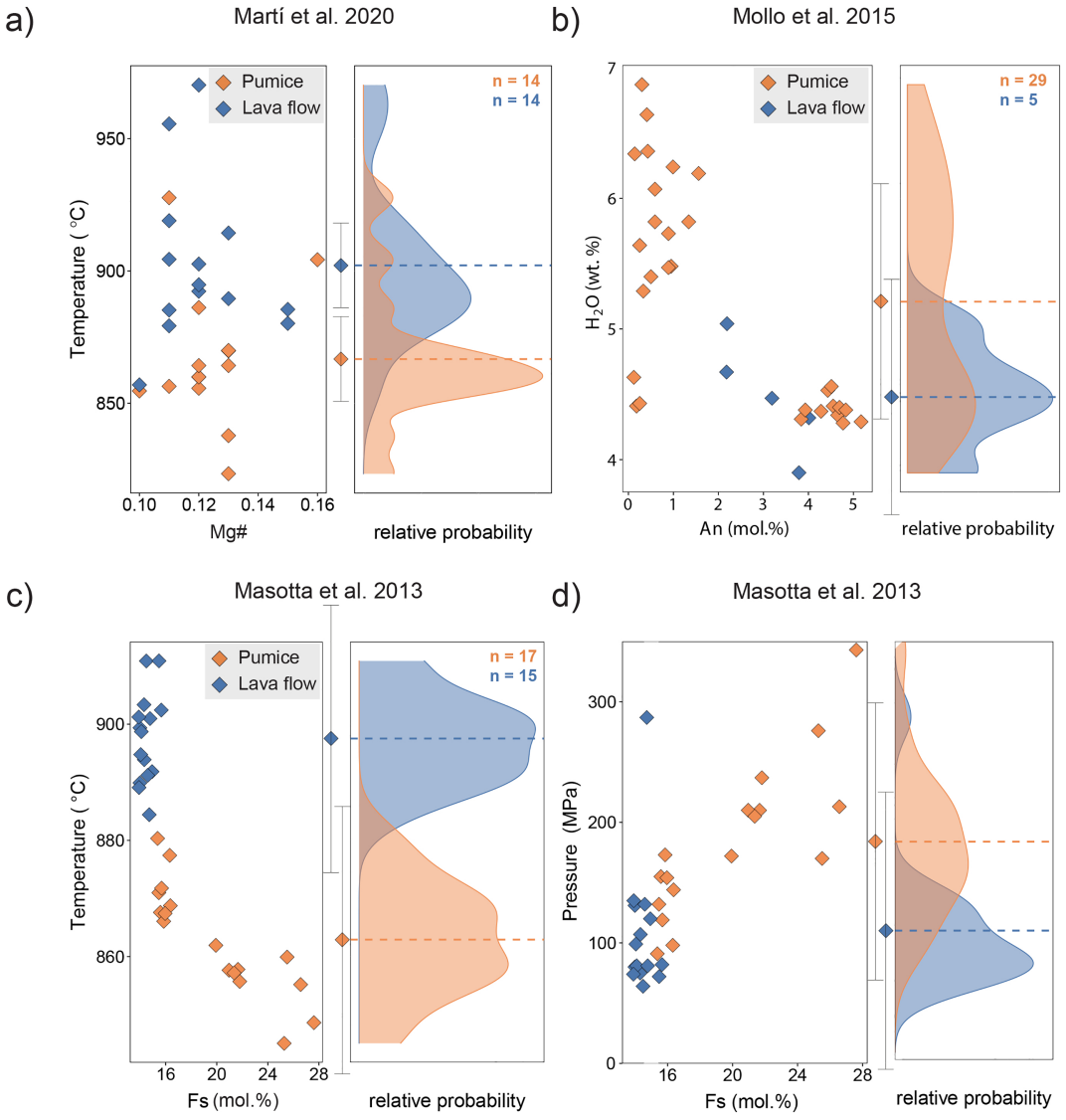
a)
Martí et al. 2020
Pumice
Lava flow
n = 14
n = 14
Temperature (°C)
950
900
850
0.10
0.12
0.14
0.16
Mg#
relative probability
b)
Mollo et al. 2015
Pumice
Lava flow
n = 29
n = 5
H2O (wt.%)
7
6
5
4
0
1
2
3
4
5
An (mol.%)
relative probability
c)
Masotta et al. 2013
Pumice
Lava flow
n = 17
n = 15
Temperature (°C)
900
880
860
16
20
24
28
Fs (mol.%)
relative probability
d)
Masotta et al. 2013
Pressure (MPa)
300
200
100
0
16
20
24
28
Fs (mol.%)
relative probability

Figure 11

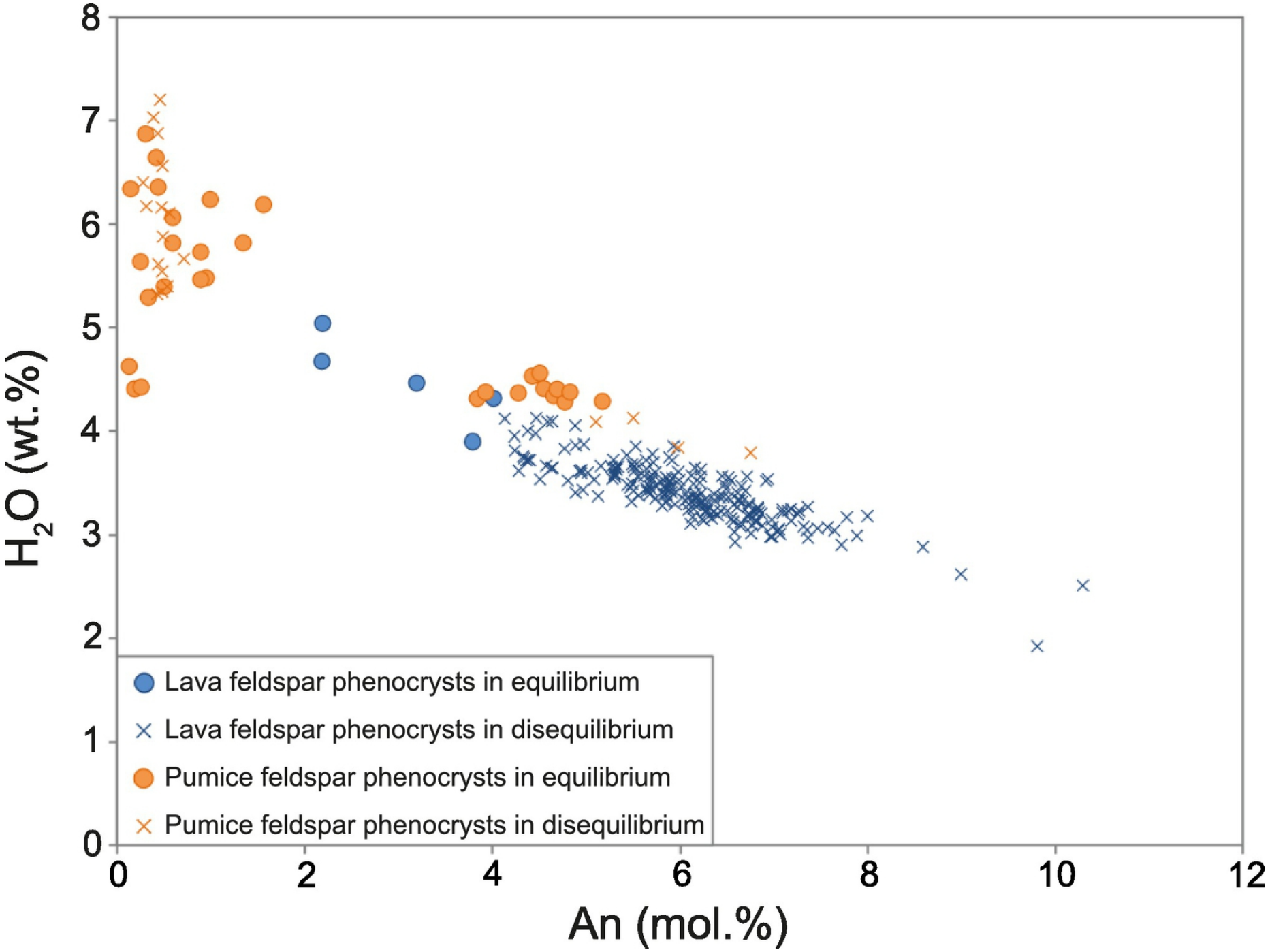
8
7
6
5
4
3
2
1
0
H_2O (wt.%)
0
2
4
6
8
10
12
An (mol.%)
Lava feldspar phenocrysts in equilibrium
Lava feldspar phenocrysts in disequilibrium
Pumice feldspar phenocrysts in equilibrium
Pumice feldspar phenocrysts in disequilibrium

Figure 12

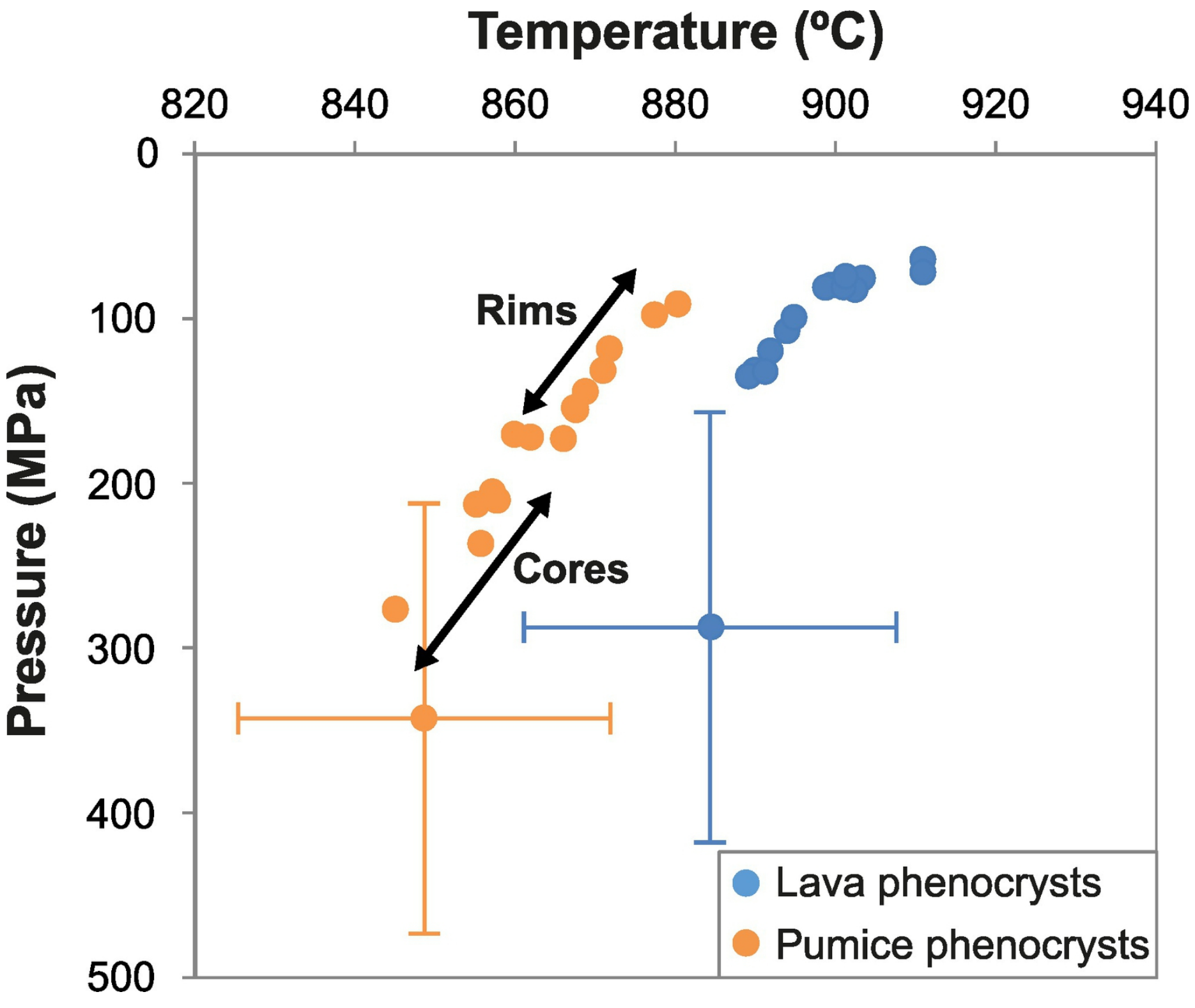
Temperature (ºC)
820
840
860
880
900
920
940
0
100
200
300
400
500
Pressure (MPa)
Rims
Cores
Lava phenocrysts
Pumice phenocrysts

Figure 13

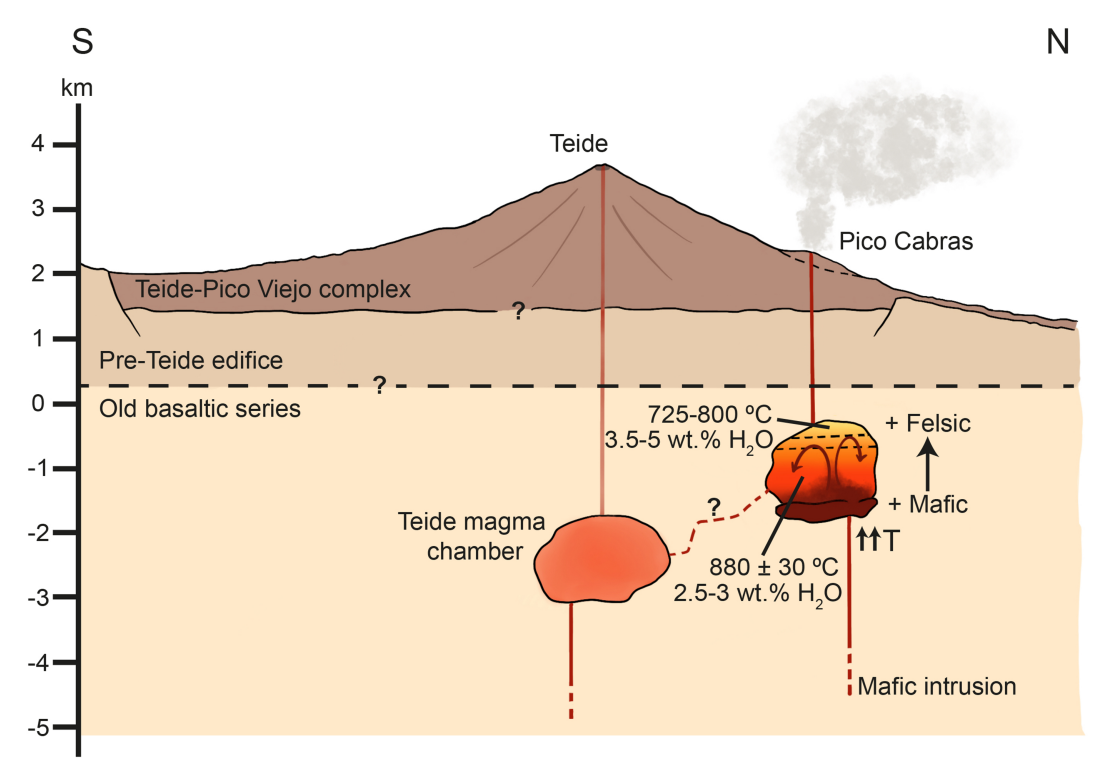
S
N
km
4
3
2
1
0
-1
-2
-3
-4
-5
Teide
Pico Cabras
Teide-Pico Viejo complex
?
Pre-Teide edifice
?
Old basaltic series
725-800 ºC
3.5-5 wt.% H2O
+ Felsic
+ Mafic
↑↑T
?
Teide magma chamber
880 ± 30 ºC
2.5-3 wt.% H2O
Mafic intrusion

Figure 14